

FUNCTIONAL MRI

Background, Methodology, Limits, and Implementation

PETER A. BANDETTINI, RASMUS M. BIRN, & KATHLEEN M. DONAHUE

Introduction

Over the past decade, magnetic resonance imaging (MRI) has developed into a powerful diagnostic technique, advancing rapidly from the creation of the first images in 1973 [1] to the current state of providing detailed information about both anatomy and function. This explosive growth is partially due to the fact that many tissue parameters can affect the MR signal. Signal acquisition can be manipulated in a variety of ways, enabling the user to control image contrast. More recently, advances in scanner hardware have enabled the collection of an entire image in 50 msec or less. Consequently, MRI has evolved from a technique able to provide images with superb soft tissue contrast to one that is also capable of imaging fast physiological processes.

The goal of this chapter is to provide the conceptual background for understanding MRI, with a particular emphasis on functional MRI (fMRI) contrast mechanisms, methods, and pertinent issues. The next section introduces the basic principles of MR imaging – that is, the creation of spatial information using magnetic field gradients. This includes a brief overview of conventional, fast, and echo planar imaging sequences, followed by a discussion of the use of these sequences to evaluate function. We then devote an entire section to explaining the use of MRI to observe human brain function.

Basic Principles of Magnetic Resonance Imaging

MAGNETIC RESONANCE PHENOMENON

Nuclei in a Magnetic Field

The first step in creating a magnetic resonance image is placing the subject in a strong magnetic field. The magnet set-up is shown in Figure 1. This field is typically in

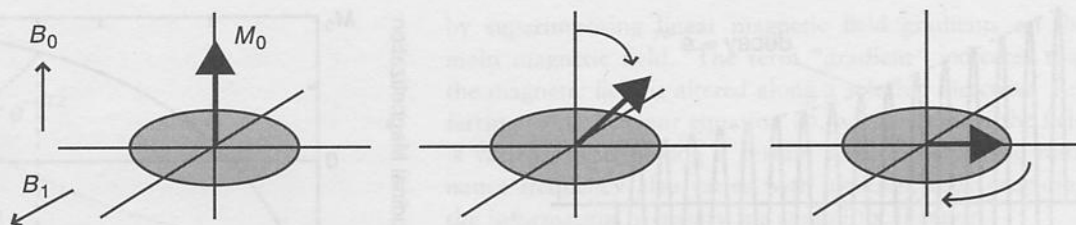
the range of 0.5 to 3 Tesla, which is ten to sixty thousand times the strength of the earth's magnetic field. The presence of such a strong magnetic field causes the nuclear spins of certain atoms within the body – namely, those with a nuclear spin dipole moment – to orient themselves either parallel or antiparallel to the main magnetic field (B_0). The nuclei precess about B_0 with a frequency, called the resonance or Larmor frequency (ν_0), which is directly proportional to B_0 :

$$\nu_0 = \gamma B_0, \quad (1)$$

where γ is the gyromagnetic ratio, a fundamental physical constant for each nuclear species. Since the proton nucleus (^1H) has a high sensitivity for its MR signal (a result of its high gyromagnetic ratio, 42.58 MHz/Tesla) and a high natural abundance, it is currently the nucleus of choice for magnetic resonance imaging. Because the parallel state is the state of lower energy, slightly more spins reside in the parallel configuration. This creates a net magnetization, which is represented by the vector M_0 .

Radiofrequency Field

Magnetic resonance occurs when a radiofrequency (RF) pulse, applied at the Larmor frequency, excites the nuclear spins and so raises them from their lower to higher energy states. Classically, this can be represented by a rotation of the net magnetization M_0 away from its rest or equilibrium state. The amount of this rotation is given in terms of the *flip angle*, which depends on the strength and duration of the RF pulse. Common flip angles are 90° , where the magnetization is rotated into a plane perpendicular to B_0 to create transverse magnetization (M_T), and 180° , where the magnetization is inverted or aligned antiparallel to B_0 . A vector diagram of magnetization during a 90° pulse is schematically shown in Figure 2. Once the magnetization is deflected, the RF field is switched off



and the magnetization once again freely precesses about the direction of B_0 . According to Faraday's law of induction, this time-dependent precession will induce a current in a receiver coil, the RF coil. The resultant exponentially decaying voltage, referred to as the free induction decay (FID), constitutes the MR signal. The FID is shown in Figure 3. Since precession occurs at the Larmor frequency, the resulting MR signal also oscillates at a frequency equal to the Larmor frequency.

During the period of free precession the magnetization returns to its original equilibrium state by a process known as *relaxation*, which is characterized by two time constants, T_1 and T_2 . These constants depend on certain physical and chemical characteristics unique to tissue type, therefore contributing substantially to the capability of MRI to produce detailed images of the human body with unprecedented soft tissue contrast.

Relaxation Phenomenon

Spin-Lattice Relaxation (T_1). Radiofrequency stimulation causes nuclei to absorb energy, lifting them to an excited state. The nuclei in their excited state can return to the ground state by dissipating their excess energy to the lattice. This return to equilibrium is termed spin-lattice relaxation and is characterized by the time constant T_1 , the spin-lattice relaxation time. The term "lattice" de-

Figure 2. A series of vector diagrams illustrating the excitation of a collection of spins by applying an alternating magnetic field, in this case a 90° radiofrequency (RF) pulse (represented here as B_1); B_0 indicates the direction of the main magnetic field. The first two vector diagrams are in a frame of reference rotating with the radiofrequency pulse. As a result, the alternating magnetic field can be represented by a vector in a fixed direction. Application of the RF pulse flips the magnetization into the transverse plane, after which the magnetization continues to precess about the main magnetic field.

scribes the magnetic environment of the nuclei. To better understand T_1 relaxation, consider the following example. Suppose that, in the equilibrium state, M_0 is oriented along the z -axis. A 90° RF pulse rotates M_0 completely into the transverse plane so that M_z (the z component of M_0) is now equal to zero. After one T_1 interval, $M_z = 0.63M_0$. After two T_1 intervals, $M_z = 0.86M_0$, and so on. Thus, the T_1 relaxation time characterizes the exponential return of the M_z magnetization to M_0 from its value following excitation.

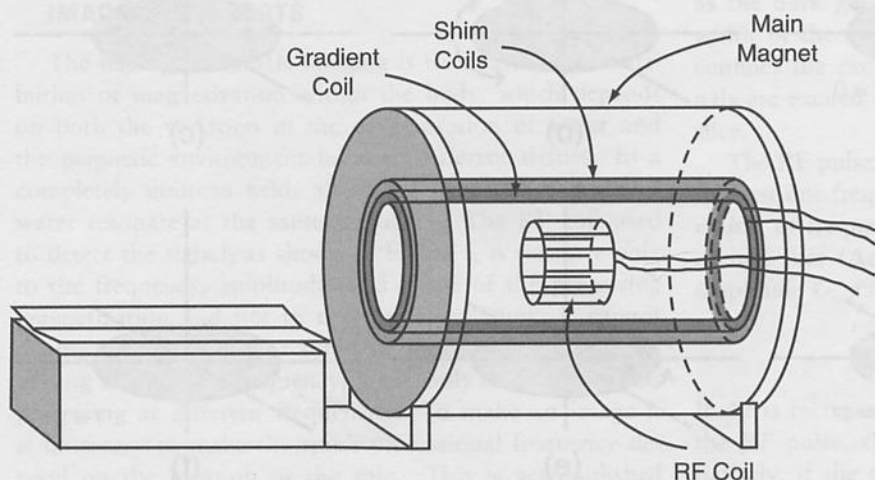
The inversion recovery sequence that is most sensitive to T_1 effects consists of a 180° RF pulse followed by a delay (TI , the inversion time), which in turn is followed by a 90° RF pulse and signal acquisition (AQ). Hence, this sequence is denoted by

$$180^\circ - TI - 90^\circ - AQ. \quad (2)$$

At time $t = 0$, M_0 is inverted by a 180° pulse, after which $M_z (= M_0)$ lies along the negative z -axis. Because of spin-lattice relaxation, M_z will increase in value from $-M_0$ through zero and back to its full equilibrium value of $+M_0$. A 90° pulse is applied at a time TI after the initial 180° pulse. The 90° pulse rotates the partially recovered magnetization, M_z , into the transverse plane, resulting in a detectable MR signal or FID. The FID reflects the magnitude of M_z after a time TI . By varying the TI , the rate of return of M_z to its equilibrium position can be monitored, as shown in Figure 4. If we assume that M_z is initially equal to $-M_0$ after the 180° pulse and recovers with an exponential decay rate $1/T_1$, then the equation describing the recovery of M_z is given by

$$M_z(t) = M_0[1 - 2e^{-t/T_1}]. \quad (3)$$

Figure 1. A schematic of a typical MR imaging system. The essential components include the magnet producing the main magnetic field, shim coils, a set of gradient coils, an RF coil, and amplifiers and computer systems (not shown) for control of the scanner and data acquisition.



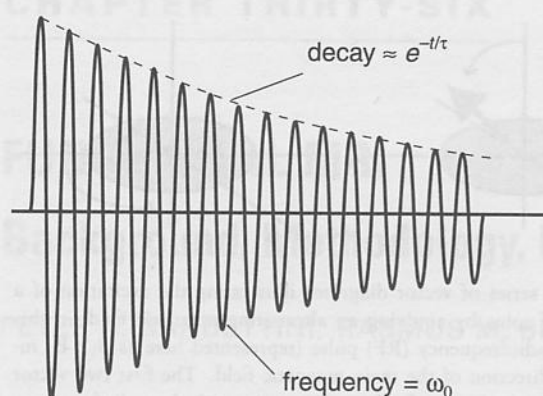


Figure 3. The signal acquired after excitation in the absence of applied magnetic field gradients is a decaying sinusoid, called the free induction decay (FID). This signal is characterized by two parameters – the amplitude and the frequency, which depend on the number and type of spins being studied and the magnetic environment that the spins are in.

Spin-Spin Relaxation (T_2 , T_2^*). Immediately after an RF pulse, the magnetic moments (or spins) are in phase. Because of natural processes that cause nuclei to exchange energy with each other, the spins lose their phase coherence. As a result, the net transverse magnetization (M_T) decays to zero exponentially with time, yielding spin-spin relaxation. This decay is characterized by the time constant T_2 . However, processes other than inherent spin-spin interactions also cause the spins to dephase. The main magnetic field is not perfectly homogeneous, so nuclei in different portions of the sample experience different values of B_0 and precess at slightly different frequencies. This is described in more detail later. When both natural processes and magnetic imperfections contribute to M_T decay, the decay is characterized by the time constant T_2^* , which

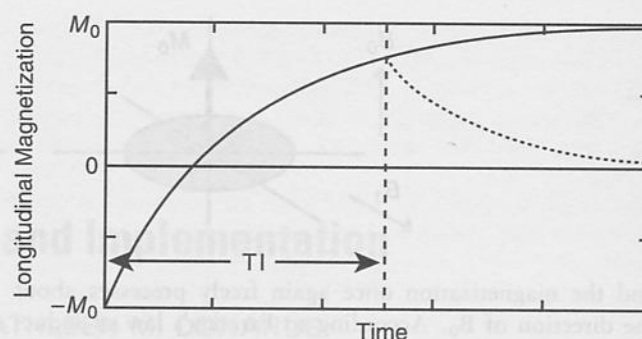


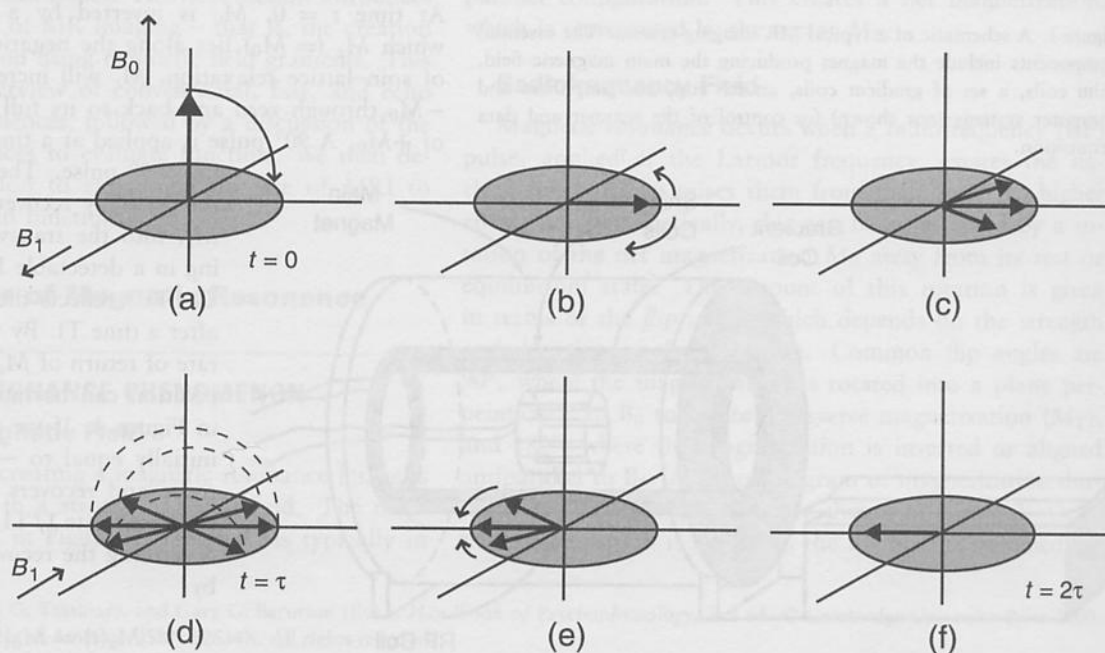
Figure 4. In an inversion recovery sequence, an initial 180° RF pulse flips the magnetization along the $-z$ -axis. The magnetization then relaxes back to its equilibrium state with a time constant T_1 . At a time T_1 after the 180° pulse, a 90° pulse is applied, flipping the partially recovered magnetization into the transverse plane. This acquired signal (dotted line) is modulated by the T_1 relaxation of the tissue.

is less than T_2 . Typically, both T_2^* and T_2 are much less than T_1 .

The spin-echo pulse sequence was designed to correct for the transverse decay due to field inhomogeneities. It consists of a 90° RF pulse followed by a 180° RF pulse and signal acquisition:

$$90^\circ - \tau - 180^\circ - \tau - \text{AQ.} \quad (4)$$

Figure 5. A series of vector diagrams illustrating the formation of a spin echo. The diagrams are shown in a frame of reference rotating with the resonance frequency of water. The magnetization is excited by an RF pulse, flipping it into the transverse plane (a). Because of magnetic field inhomogeneities, the spins dephase – shown here as a “fanning out” of the vector (b). At a time t (c), a 180° RF pulse is applied that flips the spins to the other side of the transverse plane (d). The spins then continue to precess as before, but now the slower precessing spins are ahead of the faster ones (e). The spins refocus, forming an echo of the original transverse magnetization at time $2t$ (f).



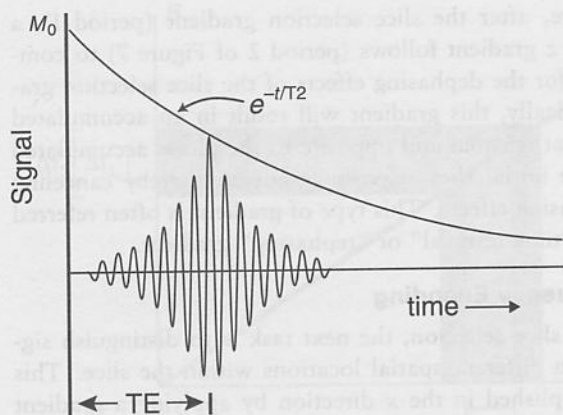


Figure 6. In a spin-echo sequence, the amplitude of the acquired signal (shown here as a spin echo) is modulated by the T2 relaxation of the spins. Signals acquired at a longer TE will be smaller.

As illustrated in Figure 5, following the 90° RF pulse, spins experiencing the slightly higher fields precess faster than those experiencing the lower fields. Consequently, the spins “fan out” or lose coherence. Then, at some time τ after application of the 90° pulse, a 180° pulse is applied and the spins will be flipped into mirror image positions; that is, the fast spins will now trail the slow spins. Hence, at a time τ later, the fast spins will have caught up with the slow spins, so that all are back in phase and a *spin echo* is created. The total period between the initial 90° pulse and the echo is denoted the echo time ($TE = 2\tau$). Thus, the spin echo reflects the magnitude M_T after time TE.

Spins lose phase coherence not only because of field inhomogeneities but also because of the natural processes responsible for spin-spin relaxation. These natural processes are irreversible and cannot be refocused. Therefore, the spin-echo signal amplitude at time TE reflects T2 decay. Consequently, as the value of TE is increased, the echo amplitudes will decrease. This is shown in Figure 6 and can be simply described as follows:

$$M_T(t) = M_0 e^{-t/T_2}. \quad (5)$$

IMAGING CONCEPTS

The basic goal of MR imaging is to measure the distribution of magnetization within the body, which depends on both the variation in the concentration of water and the magnetic environment between different tissues. In a completely uniform field, all of the hydrogen protons of water resonate at the same frequency. The RF coil used to detect the signal, as shown in Figure 1, is sensitive only to the frequency, amplitude, and phase of the precessing magnetization and not to the spatial location. It cannot distinguish two spins at different locations that are precessing at the same frequency; it can only distinguish spins precessing at different frequencies. To make an image it is necessary to make the spin's precessional frequency depend on the location of the spin. This is accomplished

by superimposing linear magnetic field gradients on the main magnetic field. The term “gradient” indicates that the magnetic field is altered along a selected direction. Referring to the Larmor equation (1), we note that if the field is varied linearly along a certain direction then the resonance frequency also varies with location, thus providing the information necessary for spatial localization.

We will first review the conventional method by which gradients are applied to acquire a two-dimensional image. Understanding these principles will aid in the understanding of more advanced techniques (e.g., fast gradient echo and echo planar imaging) that are described in subsequent sections.

Obtaining a two-dimensional image requires three steps. The first step is to excite only the spins in the slice of interest; this is called *slice selection*. The next steps are to localize the spins within that slice using the techniques of *frequency encoding* and *phase encoding*. For convenience, let z denote the direction for slice selection, x the direction for frequency encoding, and y the direction for phase encoding. These designations are arbitrary and unrelated to the actual physical orientation of the x , y , and z gradient coils. These concepts are introduced by building up a conventional spin-echo imaging sequence, which consists of a combination of RF and gradient pulses.

Slice Selection

The first step is the selection of a slice, which is achieved by applying a magnetic field gradient along the z -axis (G_z) during a 90° RF pulse of a specific frequency bandwidth (period 1 of Figure 7). When the slice selection gradient G_z is applied along the z -axis, the resonance frequencies of the protons become linearly related to positions along the z -axis. Individual resonance frequencies correspond to individual planes of nuclei. In this example, these planes are oriented perpendicular to the z -axis. When the frequency-selective 90° pulse is applied while G_z is energized, only nuclei in the plane with corresponding frequencies will be excited; thus, a slice will be selected. This is indicated as the dark gray area in Figure 8. The frequency bandwidth of the excitation pulse, together with the gradient, confines the excitation to the nuclei in the slice. No signals are excited or detected from areas outside the defined slice.

The RF pulse that is transmitted to the patient contains not just one frequency but rather a narrow range, or *bandwidth*, of frequencies. Quantitatively, the thickness of the excited slice (Δz) in centimeters is related to the gradient amplitude G_z and RF bandwidth Δf as follows:

$$\Delta z = \Delta f / \gamma G_z. \quad (6)$$

If Δf is increased so that more frequencies are present in the RF pulse, then a larger slice will be excited. Alternatively, if the strength of the gradient is decreased then

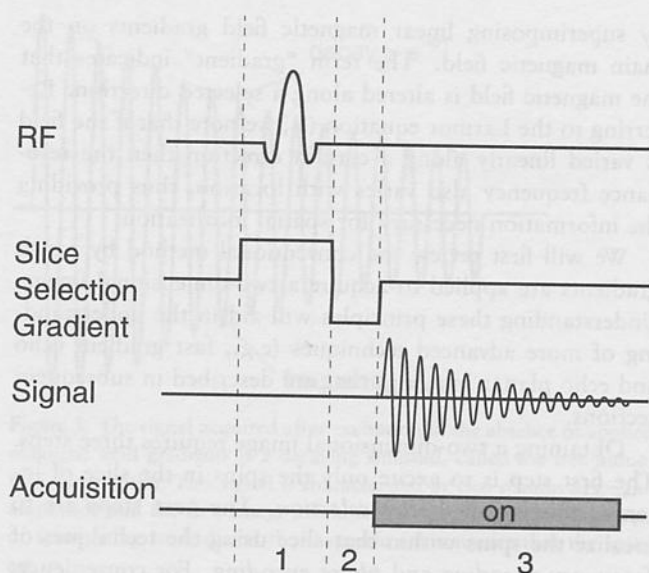


Figure 7. The sequence of RF power and gradient strength used for slice selection. To excite only one slice, a magnetic field gradient is applied during the excitation RF pulse.

more spins are resonating in a given range of frequencies, and again a larger slice is excited. Therefore the thickness of the slice excited can be varied in two ways: by changing the strength of the gradient, as indicated in Figure 9, or by varying the bandwidth of the transmitted RF pulse, as shown in Figure 10.

The slice-selection gradient G_z has two effects on the MR signal, the desired one of aiding in spatial localization and the unwanted one of dephasing the signal (since the phase of the spins is also proportional to field strength).

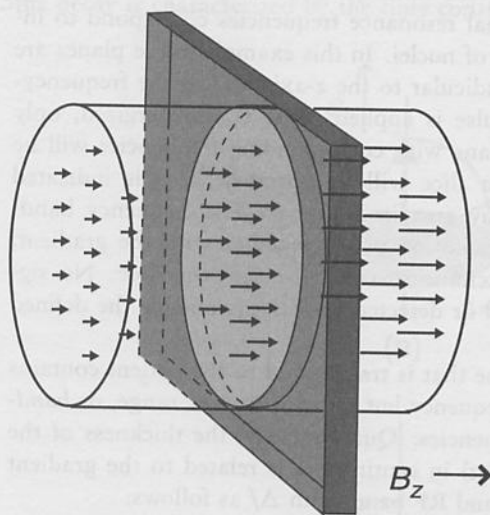


Figure 8. The application of a magnetic field gradient in slice selection creates a stronger magnetic field at one end of the sample than at the other end, shown here as arrows of varying length. When the RF pulse is transmitted into the sample, only those spins whose precessional frequency matches the frequencies in the RF pulse are excited, shown here as a dark gray slab.

Therefore, after the slice selection gradient (period 1), a negative z gradient follows (period 2 of Figure 7) to compensate for the dephasing effects of the slice selection gradient. Ideally, this gradient will result in an accumulated phase that is equal and opposite to the phase accumulated from the initial slice selection gradient, thereby canceling its dephasing effects. This type of gradient is often referred to as a "time-reversal" or "rephasing" gradient.

Frequency Encoding

After slice selection, the next task is to distinguish signals from different spatial locations within the slice. This is accomplished in the x direction by applying a gradient G_x , the *frequency encoding* gradient, during the acquisition of the signal (time period 3 in Figure 11). Because the MR signal is sampled during the time that G_x is on, this period is also commonly referred to as the "readout" period and G_x as the "read" gradient. This signal can come from either the FID or a spin-echo sequence, the latter formed by applying a 180° pulse at a time $TE/2$ after the 90° excitation pulse, as shown in Figure 11(b). Sequences that collect the signal from the FID are known as gradient-echo (GRE) sequences; those that collect the signal from the spin echo are known as spin-echo (SE) sequences. The two differ in the contrast that they provide. For example, because of the refocusing pulse, spin-echo sequences are less susceptible to magnetic field inhomogeneities and thus reflect differences in T_2 rather than T_2^* relaxation times between the tissues. These differences will be discussed in detail later. The next few sections will deal mainly with the spin-echo sequence.

The way in which the linear gradient encodes the spatial information can be more easily seen by considering a sample consisting of two vials of water, aligned with the y -axis and placed some distance apart in the x direction (see Figure 12). All of the signal comes from these two sources of water. If signal from this sample is collected without the application of any gradients, both areas are

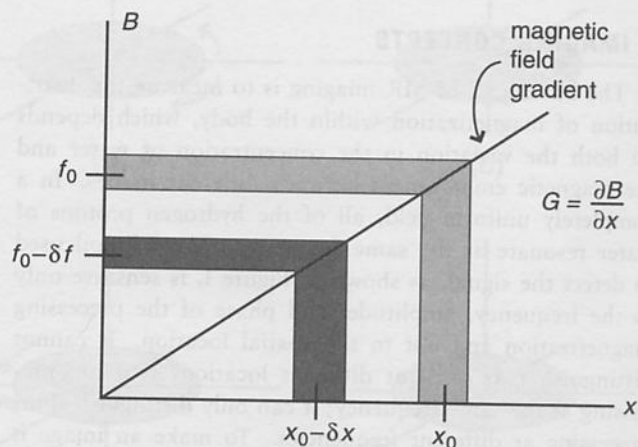
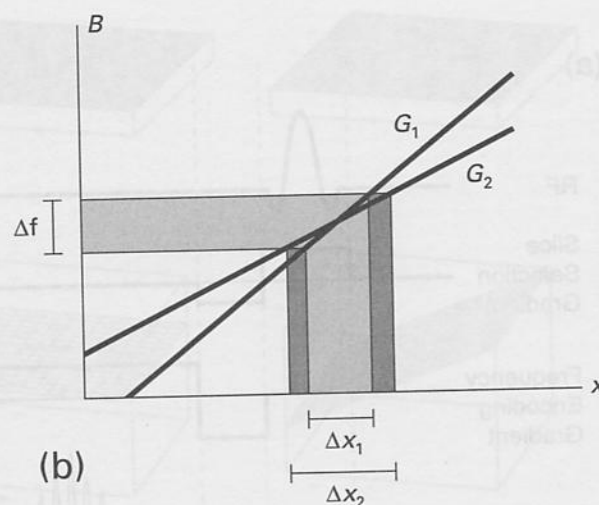
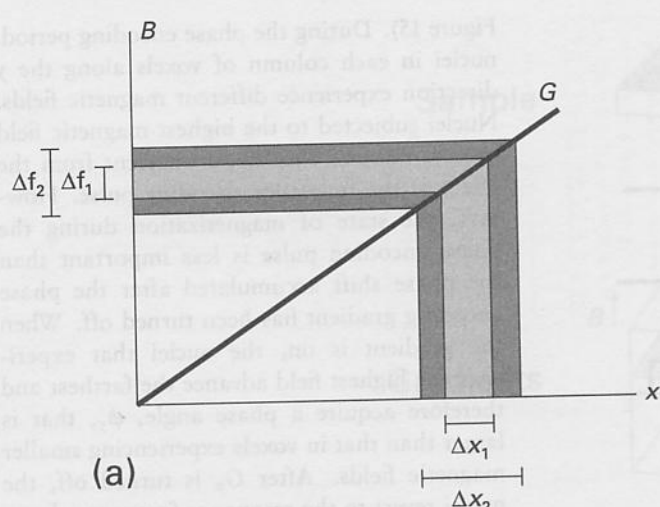


Figure 9. The position of the excited slice can be varied by changing the frequency of the transmitted RF pulse.



precessing at the same frequency. Consequently, the signal will appear as a pure sinusoid, and applying a mathematical process called the Fourier transform will show that it contains only one frequency. (Whereas the FID represents the time evolution of M_{xy} , the Fourier transform of the signal represents its frequency distribution.) The amplitude of this frequency peak corresponds to the total amount of water from both vials.

However, if a gradient is applied during the acquisition of the signal, then the spins in one vial are in a slightly higher magnetic field than those in the other vial. According to the Larmor relation, one group of spins will precess faster than the other group, and the signal will be an interference pattern composed of both of these frequencies. A Fourier transform applied to this signal will reveal two distinct frequencies. Since a spatially linear gradient was applied, the frequencies of these peaks exactly correspond to the position of the vials. Also, the amount of signal at a given frequency is determined by the number of spins precessing at that frequency, so it is directly related to the amount of magnetization at a given location. In other words, the Fourier transform of the signal is simply a projection of the distribution of magnetization onto the frequency encoding axis.

Figure 13 shows the phases of the magnetization vectors in one slice at three time points during frequency encoding. The presence of the gradient induces the spins at one end to precess faster than those at the other end, causing an increasing amount of phase shift along this direction. As time progresses (when the gradient has been applied for a longer duration), the amount of "phase twisting" is increased. One effect of this is that the peak of the signal (when it is least dephased) will be at the beginning of the acquisition. In order to move the peak signal to the center of the acquisition window, a negative gradient lobe (time reversal gradient) with exactly half the area of the frequency encoding gradient is applied just *before* the frequency encoding gradient. This initially dephases

Figure 10. The thickness of the excited slice can be varied either by (a) changing the bandwidth of the transmitted RF pulse or by (b) changing the amplitude of the slice selection gradient. Here Δf_1 = frequency 1, corresponding to slice thickness Δx_1 ; Δf_2 = frequency 2, corresponding to slice thickness Δx_2 ; and G = magnetic field gradient.

the spins, which are then brought back in phase by the applied frequency encoding gradient (see Figure 14). In the spin-echo sequence, the gradient lobe is positive and occurs before the 180° inversion pulse.

The details of the frequency encoding procedure dictate the image size (in centimeters) or *field of view* along the x -axis:

$$\text{FOV}_x = \frac{\text{BW}}{\gamma G_x}, \quad (7)$$

where BW is the receiver bandwidth. Note that the receiver bandwidth should not be confused with the excitation RF bandwidth, which dictates the slice thickness (see equation (6)). Here, the bandwidth is the effective range of frequencies that can be properly detected, as determined by the Nyquist criterion [2]. The BW is controlled by the digital sampling rate, which in turn is determined by the number of points N_x on the signal to be digitized and the length of time the receiver is on (the acquisition time, AQ):

$$\text{BW} = \frac{N_x}{\text{AQ}}. \quad (8)$$

Accordingly, from these two equations, the pixel size along the frequency encoding axis can be derived as follows:

$$\text{pixel size} = \frac{\text{FOV}_x}{N_x} = \frac{1}{\gamma G_x (\text{AQ})}. \quad (9)$$

Phase Encoding

The final spatial dimension can be encoded into the signal by applying a programmable phase encoding gradient G_y , simultaneous with the rephasing gradient in period 2, in the time between the excitation and the acquisition (see

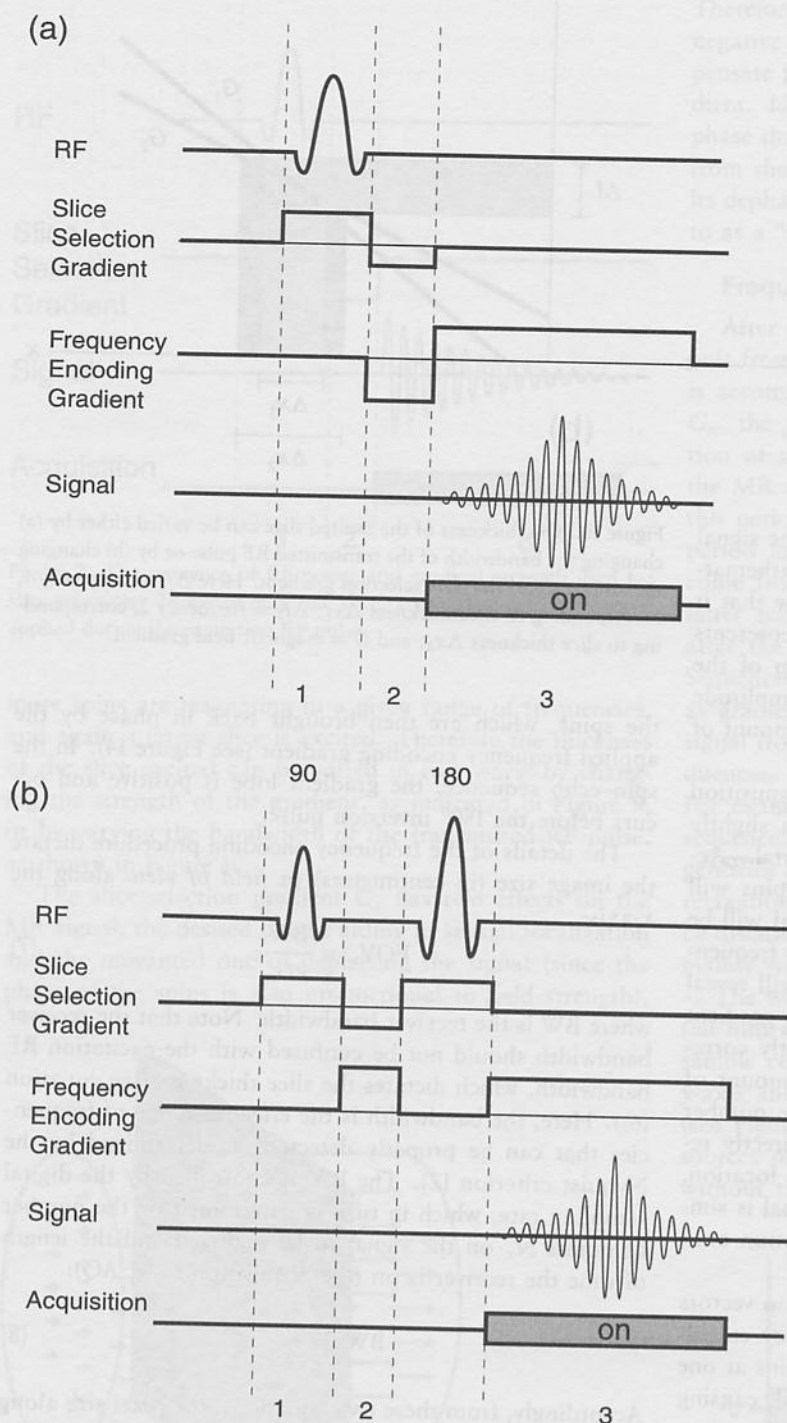


Figure 11. The sequence of RF power and gradient amplitudes used to excite one slice and encode the positions of the spins within that slice into the signal. In this *frequency encoding*, the positions of the spins are encoded by applying a magnetic field gradient in one of the directions in the excited slice during the acquisition. Note that the signal can come either from (a) the FID or (b) a spin echo (an echo of the FID). Sequences using signals from the FID are called gradient-echo sequences; sequences using signals from the spin echo are called spin-echo sequences.

Figure 15). During the phase encoding period, nuclei in each column of voxels along the y direction experience different magnetic fields. Nuclei subjected to the highest magnetic field precess fastest. This is no different from the effect of the frequency encoding pulse. However, the state of magnetization during the phase encoding pulse is less important than the phase shift accumulated after the phase encoding gradient has been turned off. When the gradient is on, the nuclei that experience the highest field advance the farthest and therefore acquire a phase angle, ϕ_y , that is larger than that in voxels experiencing smaller magnetic fields. After G_y is turned off, the nuclei revert to the resonance frequency determined by the main magnetic field. However, they "remember" the previous event by retaining their characteristic y -dependent phase angles. The field of view in the y direction (FOV_y) is quantitatively defined in a manner similar to (7):

$$FOV_y = \frac{1}{\gamma T_y G_{y\max}}, \quad (10)$$

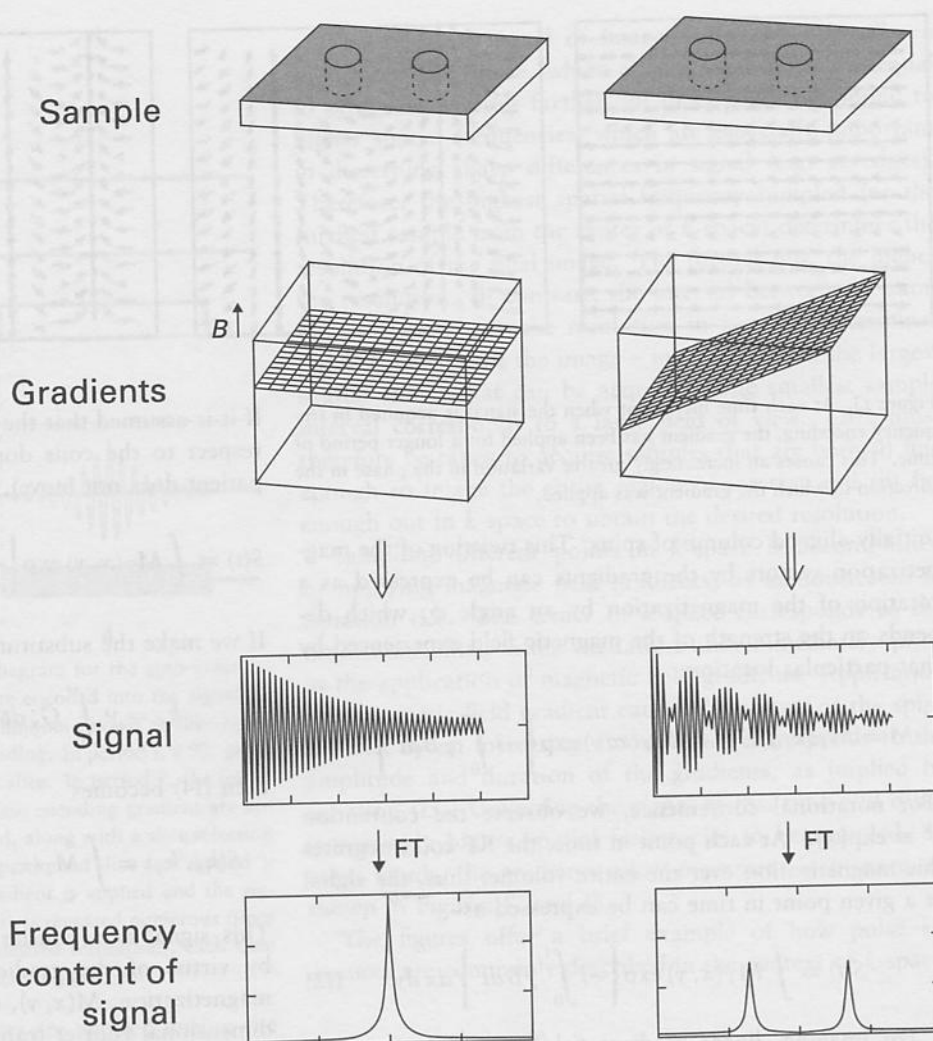
where T_y is the duration and $G_{y\max}$ is the maximum amplitude of the phase encoding gradient.

Although the signal obtained from one acquisition (slice selection, phase encoding, and frequency encoding) contains information from all voxels in the imaging slice, the information gathered from a single iteration of this sequence is not sufficient to reconstruct an image. Consequently, the sequence must be repeated with different settings of the phase encoding gradient G_y .

When a phase encoding gradient of a particular value has been applied, the effect of that gradient is to shift the phases of the spins by an amount depending on their position (in this case, in the y direction) and the amplitude of the phase encoding gradient. For example, spins near the isocenter experience no phase shift, whereas spins at positions off center are shifted by a certain amount depending on their distance from the center.

The net result of this spin dephasing is simply a decrease in the signal. It is only through varying the amount of this dephasing (thus varying the amount of signal decrease) – by stepping through the phase encoding gradient's range of amplitudes – that the location of structures along the phase encoding gradient can be identified.

If the data at each cycle of the G_y setting were plotted, it would show sinusoidal curves with a frequency



dictated by the rate of phase change (between each iteration of the pulse sequence), which, in turn, depends on location. A similar curve is derived during frequency encoding, but with a difference: each sample along this curve originates from a different MR signal. Each of these MR signals follows a phase encoding gradient pulse of different amplitude. However, as with frequency encoding, the frequency components of the curve are identified by the Fourier transform and the magnetization is ascribed to a given location.

In summary, for a matrix of size $N_y \times N_x$, the required number of iterations is N_y . The N_y signals, each corresponding to a different value of G_y , are sampled N_x times during the read period. Subsequent two-dimensional Fourier transformation yields the intensity values of each of the $N_y \times N_x$ pixels.

Image Formation Mathematics: k -Space

The key to image formation is encoding the location of the magnetization in the phase of the MR signal. It is worthwhile to look at this encoding process in more detail. Consider the encoding of spatial information along

Figure 12. A series of steps illustrating the concept of frequency encoding to distinguish the signal coming from two point sources of magnetization (e.g., small vials of water) in an object. *Left.* When no gradient is applied, both sources of magnetization resonate at the same frequency, and the signal is a simple decaying sinusoid. When this signal is Fourier transformed, the signal is shown to contain only one frequency. *Right.* When a gradient is applied, one of the sources of magnetization precesses at a higher frequency than the other. The resulting signal is an interference pattern of the two frequencies, which is shown (by Fourier transformation) to contain two distinct frequencies. Notice that the Fourier transformed signal is the projection of the amount of magnetization along the axis along which the gradient was applied. That is, in this one-dimensional case, the frequency content of the signal is the image.

one dimension within the plane after the slice has been excited. A collection of spins along one dimension can be thought of as a column of vectors, as shown in Figure 16. After the slice has been excited, all of the spins within the slice are in phase. Once a magnetic field gradient is applied, the spins will precess at different frequencies depending on their location. At any given moment, certain spins will have accumulated more phase than others. These gradients can thus be thought of as "twisting" the

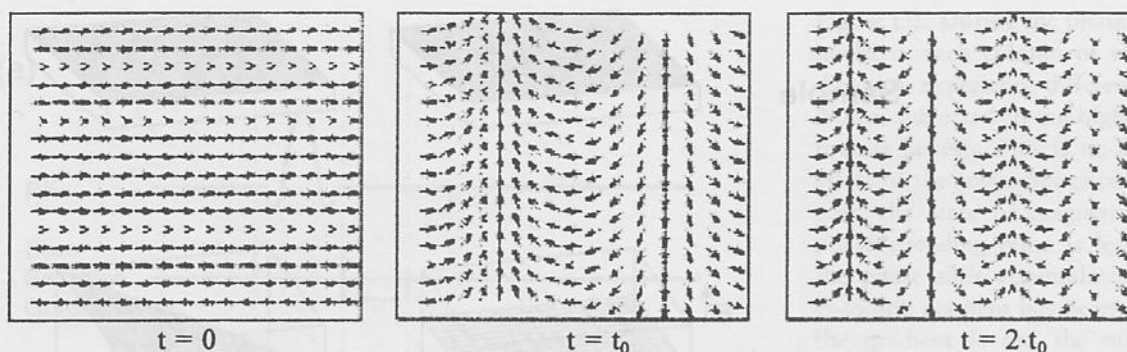


Figure 13. At each time increment when the signal is acquired in frequency encoding, the gradient has been applied for a longer period of time. This causes an increasingly greater variation in the phase in the direction in which the gradient was applied.

initially aligned column of spins. This twisting of the magnetization vectors by the gradients can be expressed as a rotation of the magnetization by an angle ϕ , which depends on the strength of the magnetic field experienced by that particular location:

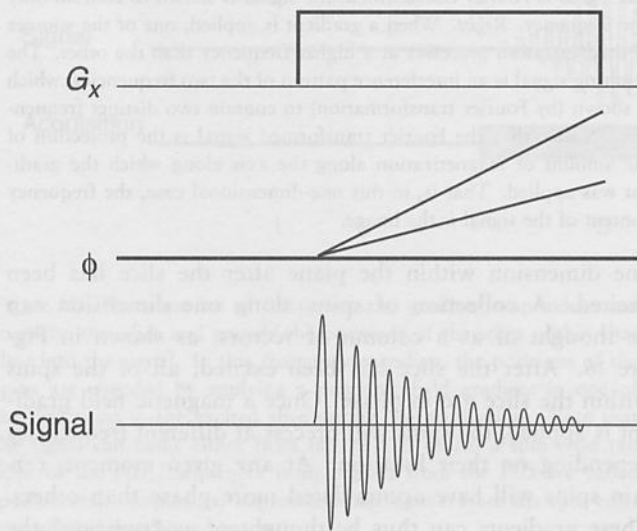
$$M = M_T(x, y)e^{-i\phi} = M_T(x, y) \exp\left\{-i \int_0^t \gamma B dt'\right\}. \quad (11)$$

(For notational convenience, we observe the convention $e^x \equiv \exp\{x\}$.) At each point in time, the RF coil integrates this magnetization over the entire volume; thus, the signal at a given point in time can be expressed as

$$S(t) = \int M_T(x, y) \exp\left\{-i \int_0^t \gamma B dt'\right\} dx dy. \quad (12)$$

For imaging, linear gradient fields are applied and so the magnetic field B experienced by the spins can be rewritten as

$$B = \int G_x dx + \int G_y dy = G_x x + G_y y. \quad (13)$$



If it is assumed that the position of the magnetization with respect to the coils does not change with time (i.e., the patient does not move), then the signal can be written as

$$S(t) = \int M_T(x, y) \exp\left\{-i\left(x\gamma \int_0^t G_x dt' + y\gamma \int_0^t G_y dt'\right)\right\} dx dy. \quad (14)$$

If we make the substitutions

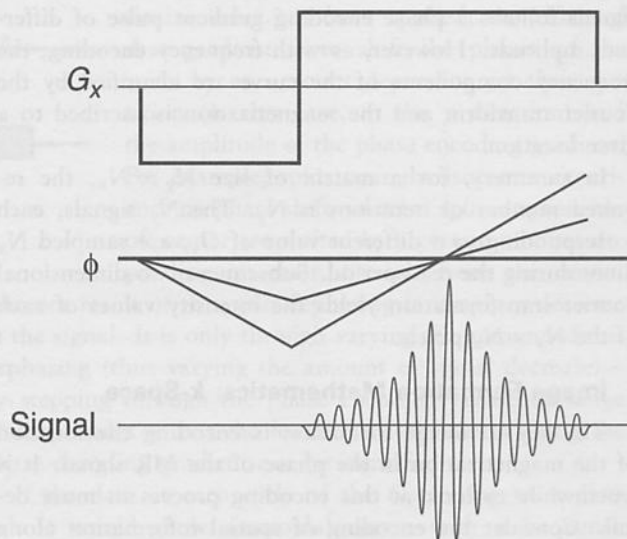
$$k_x = \gamma \int_0^t G_x dt' \quad \text{and} \quad k_y = \gamma \int_0^t G_y dt', \quad (15)$$

then (14) becomes

$$S(k_x, k_y) = \int M_T(x, y) \exp\{-i(k_x x + k_y y)\} dx dy. \quad (16)$$

This signal is a Fourier transform of the magnetization, by virtue of the gradients applied. A measure of the magnetization, $M(x, y)$, can be obtained by taking a two-dimensional Fourier transform of the signal.

Figure 14. Diagrams showing the gradient amplitude, the phase of two spins subjected to these gradients, and the profile of the resulting signal. When an initial negative gradient is applied (right), the spins are in phase in the center of the acquisition window. This leads to a greater net signal.



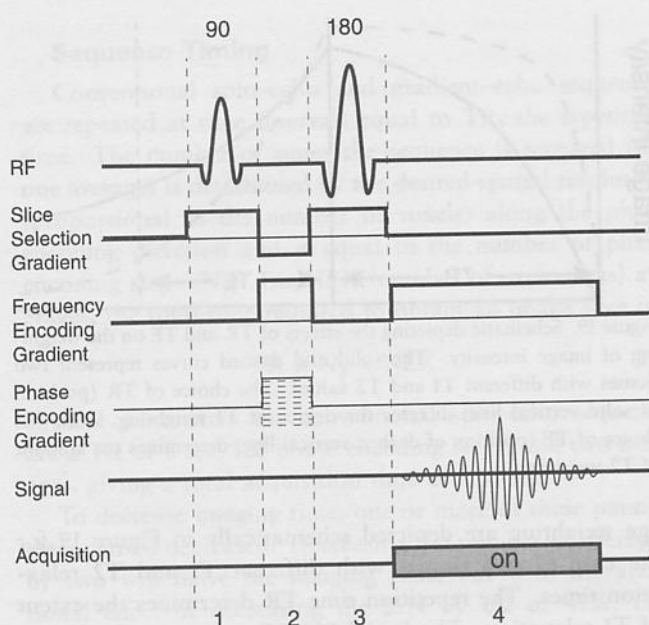


Figure 15. A complete pulse sequence diagram for the spin-echo sequence. Spatial locations of the spins are encoded into the signal by applying three orthogonal gradients, techniques known as slice selection, frequency encoding, and phase encoding. In period 1, a 90° pulse and a slice selection gradient excite one slice. In period 2, the initial frequency encoding gradient and the phase encoding gradient are applied. In period 3, a 180° pulse is applied, along with a slice selection pulse (such that only the spins in the same excited slice are "flipped"); in period 4, the frequency encoding gradient is applied and the signal is acquired. The sequence shown here is repeated numerous times (128, 256, 512, etc., depending on the desired resolution), each time with a different strength of the phase encoding gradient.

Because of the way the gradients are applied during the imaging scan, it is natural to think of the MR signal as being collected in spatial frequency space, or " k -space" [3–5], as implied by the terms in equation (15). This representation is often much more convenient in discussing the details of pulse sequences. In this space, usually plotted in two dimensions, each point describes the amount of a particular spatial frequency present in the imaged object.

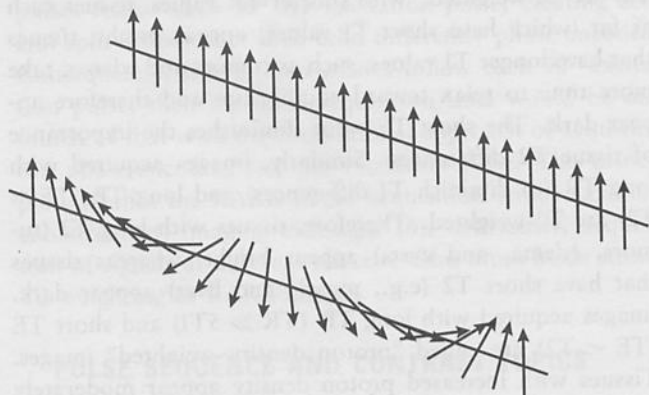


Figure 16. The application of a magnetic field gradient can be thought of as twisting the initially aligned column of spins. These spins are then summed at every point in time using the RF coil.

The strongest signal of imaged objects is typically in the center of k -space, where all gradient values are equal to zero. The regions farther out in k -space correspond to higher spatial frequencies, which are especially important in discerning sharp differences in signal (e.g. at edges). Therefore, the highest spatial frequency sampled (or the furthest sample from the center of k -space) determines the resolution of the final image. The further out, the higher the resolution. In contrast, the interval between the samples in k -space, or the resolution in k -space, determines the field of view of the image – in other words, the largest spatial extent that can be acquired. The smallest sample interval corresponds to a large field of view. Care must therefore be taken to acquire samples that are both (i) fine enough to image the entire region of interest and (ii) far enough out in k -space to obtain the desired resolution.

Sampling different points in k -space is accomplished by applying magnetic field gradients, as demonstrated in equation (15). The center of k -space corresponds to the time immediately after excitation and immediately prior to the application of magnetic field gradients. Application of a magnetic field gradient causes the phases of the spins to twist by an increasing amount that corresponds to the amplitude and duration of the gradients, as implied by equation (15). Collecting the signal at this time will cause increasingly higher spatial frequencies to be sampled. In other words, the gradients allow movement in k -space, as shown in Figures 17 and 18.

The figures offer a brief example of how pulse sequences are commonly described in the context of k -space.

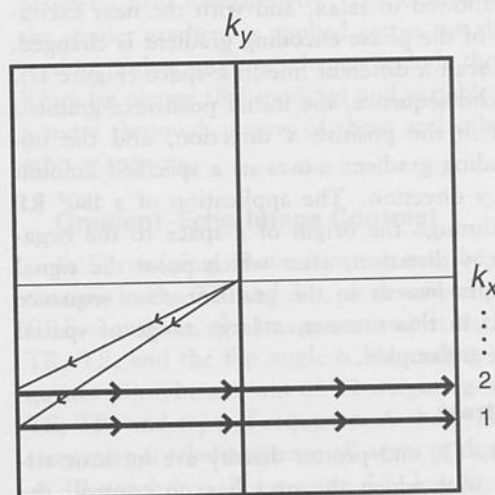


Figure 17. A k -space diagram showing the path through k -space taken to acquire the signal for the gradient-echo (GRE) sequence. For each excitation, the phase encoding gradient moves us a fixed distance in the negative k_y direction and the initial negative frequency encoding gradient moves us in the negative k_x direction. The signal is then sampled moving in the positive k_x direction as the frequency encoding gradient is applied. The signal is then allowed to relax, and the sequence is repeated with a different value for the phase encoding gradient. In this manner, a sufficient range of k -space can be scanned.

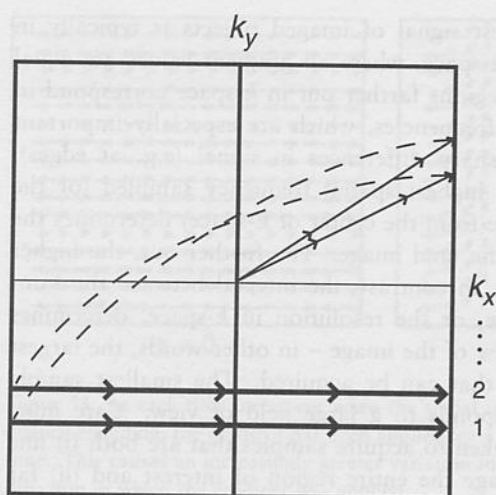


Figure 18. A k -space diagram for the spin-echo (SE) sequence. After the spins are excited, gradients in the positive x and y directions are applied, moving us in the positive k_x and positive k_y direction. The 180° pulse flips us through the center of k -space to the negative k_x , negative k_y direction, after which the positive frequency encoding gradient moves us in the positive k_x direction, allowing us to sample the frequencies as before. This sequence of steps is repeated with different values for the phase encoding gradient.

In the gradient-echo sequence described earlier, we started at the origin of k -space after the excitation. The initial negative x -gradient lobe moves us to the left (negative x frequency) and the phase encoding gradient moves us a specific amount in the y direction of k -space. The final application of an x gradient moves us in the positive x direction, during which time we acquire the signal. The signal is then allowed to relax, and with the next excitation, the value of the phase encoding gradient is changed, allowing us to scan a different line in k -space (Figure 17). For the spin-echo sequence, the initial positive x -gradient lobe moves us in the positive x direction, and the initial phase encoding gradient moves us a specified amount in the positive y direction. The application of a 180° RF pulse flips us through the origin of k -space to the negative x , negative y direction, after which point the signal acquisition occurs just as in the gradient-echo sequence (see Figure 18). In this manner, a large range of spatial frequency space is sampled.

Image Contrast

Although T_1 , T_2 , and proton density are intrinsic tissue parameters over which the user has no control, the operator can alter tissue contrast and the signal-to-noise ratio (S/N) by the choice of the pulse sequence parameters. Specifically, images can be obtained in which tissue contrast is primarily determined by (i.e. weighted toward) T_1 , T_2 , or proton density characteristics. With the spin-echo imaging sequence, for example, the type of image weighting is determined by the repetition time (TR) and the echo time (TE). The effects of TR and TE on im-

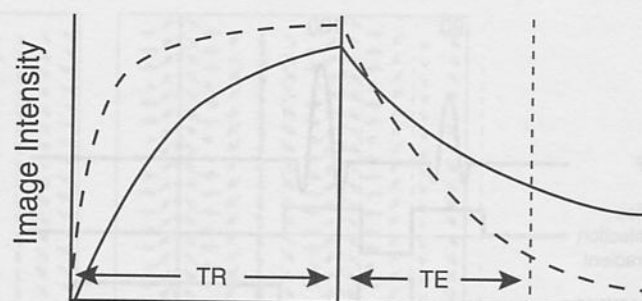


Figure 19. Schematic depicting the effects of TR and TE on the weighting of image intensity. The solid and dashed curves represent two tissues with different T_1 and T_2 values. The choice of TR (position of solid vertical line) dictates the degree of T_1 weighting, while the choice of TE (position of dashed vertical line) determines the amount of T_2 weighting.

age weighting are depicted schematically in Figure 19 for the case of two tissues with different T_1 and T_2 relaxation times. The repetition time TR determines the extent of T_1 relaxation. The initial 90° RF pulse completely tips the existing longitudinal magnetization into the transverse plane, leaving zero longitudinal magnetization. If the spins were again excited at this time, no signal would be produced. Therefore, a time interval (TR) is allowed to elapse between excitations so that the spins can undergo T_1 relaxation and recover at least part of their longitudinal magnetization.

It is apparent from Figure 19 that the maximum T_1 contrast between tissues occurs when TR is greater than zero and less than some time when both tissues have completely recovered their longitudinal magnetization. A long TR (i.e., $\gg 5T_1$) allows enough time to elapse so that almost complete T_1 relaxation occurs, rendering signal intensity not a function of T_1 . The maximum magnetization to which the signal returns is determined by proton density. Likewise, the amount of T_2 contrast is dictated by the choice of TE. The longer the time interval TE, the greater the extent of T_2 relaxation. Therefore, spin-echo images acquired with short TR ($TR \approx T_1$) and short TE ($TE < T_2$) are T_1 -weighted. With shorter TR values, tissues such as fat (which have short T_1 values) appear bright; tissues that have longer T_1 values, such as tumors and edema, take more time to relax toward equilibrium and therefore appear dark. The short TE value diminishes the importance of tissue T_2 differences. Similarly, images acquired with long TR (to diminish T_1 differences) and long TE ($TE \approx T_2$) are T_2 -weighted. Therefore, tissues with long T_2 (tumors, edema, and cysts) appear bright, whereas tissues that have short T_2 (e.g., muscle and liver) appear dark. Images acquired with long TR ($TR \gg 5T_1$) and short TE ($TE < T_2$) are called "proton density-weighted" images. Tissues with increased proton density appear moderately bright. It should be noted that both T_1 - and T_2 -weighted images are always partly weighted toward proton density as well.

Sequence Timing

Conventional spin-echo and gradient-echo sequences are repeated at time intervals equal to TR, the repetition time. The number of times the sequence is repeated (for one average) is determined by the desired spatial resolution (proportional to the number of voxels) along the phase encoding direction and is equal to the number of phase encoding steps (N_y). For NEX (number of excitations) averages, the total time required to obtain an image slice is

$$TR \times N_y \times NEX. \quad (17)$$

Typical parameters for conventional spin-echo sequence are a TR of 2 sec, 128 phase encoding steps, and two averages, giving a total acquisition time of 8.5 min.

To decrease imaging time, one or more of these parameters can be decreased. Decreasing the number of averages by two will halve the imaging time, but with the additional effect of decreasing the S/N by $\sqrt{2}$ or 41%; this will increase the graininess of the image. Motion artifacts (which are also decreased by averaging) could become significant if imaging time were reduced by decreasing the number of averages. Reducing the image matrix size or the number of phase encoding steps decreases imaging time at the expense of spatial resolution. Moreover, the larger pixels result in an increased S/N. The simplest way to speed up an ordinary SE scan would be to drastically reduce TR. However, the signal produced depends on the amount of T1 relaxation that occurs during the interval TR and thus on the available signal for the next excitation. A short TR relative to T1 would result in significant signal losses. Consequently, the T1 relaxation times of tissue protons limit the degree to which the pulse repetition times (TR) can be shortened. Two techniques that overcome TR limitations include gradient-echo (GRE) and echo planar imaging (EPI) techniques. These fast imaging sequences are discussed in the following sections.

An alternate procedure to speed up acquisition of spin-echo images has been developed in which several 180° pulses follow each 90° RF excitation pulse, creating several spin echoes with each echo differently phase encoded. Consequently, if four spin echoes follow each 90° excitation pulse, then the total acquisition time would be one fourth of that with the conventional approach of acquiring one phase encoding step per excitation pulse. This principle underlies the RARE (rapid acquisition with relaxation enhancement) imaging technique [6]. Obviously, acquisition of signals at different effective echo times lends strong T2 weighting to RARE images.

PULSE SEQUENCE AND CONTRAST TOPICS

Fast Gradient-Echo Imaging

In its most basic form, the GRE pulse sequence, as shown in Figure 11(a), consists of one RF pulse with a flip

angle α , followed at some time later by the acquisition of the gradient echo. The time between the excitation and the acquisition of the gradient echo is defined as the echo time, TE:

$$\alpha \text{ degrees} \rightarrow TE \rightarrow \text{gradient echo}. \quad (18)$$

Because GRE sequences lack a 180° refocusing pulse, images generated with these sequences are sensitive to artifacts from magnetic field inhomogeneities (i.e., T2* effects).

Gradient echo sequences are typically used as fast sequences because data are acquired before the dephasing of spins from previous application of the pulse sequences is complete; that is, T2* decay is not complete. In most cases, the TR is less than the time for more than 90% of the spins to dephase (three times the T2 time). Consequently, GRE sequences may be further divided into two categories according to how they handle the residual magnetization after data acquisition: those that attempt to maintain it in a steady-state condition and those that simply eliminate it. Those techniques that maintain it – refocused FLASH (fast low-angle shot), FISP (fast imaging with steady-state precession), and GRASS (gradient-recalled acquisition steady state) – rephase the spins along one or more axes prior to reapplication of the next RF pulse.

Gradient echo sequences that eliminate the residual transverse magnetization (e.g., spoiled FLASH or spoiled GRASS sequences) typically use a “spoiler” pulse to accelerate the dephasing (see Figure 20). Specifically, a high-amplitude, long-duration gradient ruins (spoils) the residual transverse magnetization by disturbing the local magnetic field homogeneity. The best results occur when the spoiler gradient is applied across the slice selection direction. Other spoiling schemes include the use of random RF pulse phases (RF spoiling) and variable TR. See [7] for a more thorough review of these and other fast gradient echo sequences.

Gradient-Echo Image Contrast

In SE imaging, tissue contrast may be manipulated by changes in the TR and TE, as described previously. With GRE sequences, the image contrast is varied by changing TR, TE, and the flip angle α , depending on the pulse sequence [8]. The amount of T2 weighting is dictated by the TE, TR, and type of sequence. A short TE, long TR, and transverse-spoiled sequence all serve to decrease the degree of T2 weighting. For a given TE, low flip angles increase proton density weighting whereas high flip angles increase T1 weighting. At very short TRs, however, the images become weighted toward T2/T1 – that is, structures with larger T2/T1 ratios (e.g. liquids) appear bright. Yet, with very fast GRE sequences (TR \approx 3 msec) and $\alpha < 5^\circ$, soft tissue contrast almost disappears [9]. The signal becomes dominated by spin density. However, if conventional MR experiments are placed before the whole GRE imaging

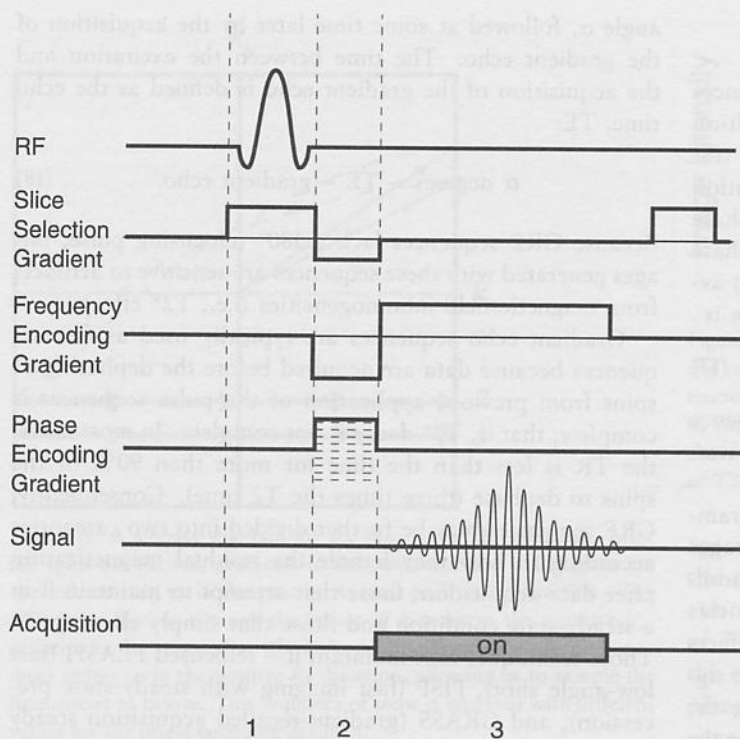


Figure 20. A complete pulse sequence diagram for a gradient-echo sequence. Spatial locations of the spins are encoded into the signal by applying three orthogonal gradients. The sequence shown here is repeated numerous times (128, 256, 512, etc., depending on the desired resolution), each time with a different strength of the phase encoding gradient. The gradient-echo sequence has an advantage over the spin-echo sequence for fast imaging in that it does not use a 180° pulse and does not rely on a 90° excitation pulse.

sequence, images of any desired contrast can be achieved without changing the measuring time. The turbo-FLASH imaging technique is one technique that implements this idea.

The turbo-FLASH method employs an initial 180° RF pulse to invert the spins. Next, an inversion delay (TI) is allowed to elapse, during which differences in longitudinal magnetization (T1 contrast) evolve depending on the T1 relaxation times of various tissues. Finally a very rapid gradient-echo acquisition using an ultrashort TR (e.g., 4 msec) and an ultrashort TE (e.g., 2 msec) is performed. The total time for data acquisition (32 phase encoding steps) is on the order of 100 msec. When using a contrast agent, an appropriate TI value can be selected so that signal from the tissue that does not receive contrast agent is eliminated; this enables wash-in of a contrast agent to be easily visualized [10].

Gradient-Echo Timing

Like the spin-echo sequence, the GRE sequence is repeated at time intervals equal to TR; the total time required to obtain an image slice is $TR \times N_y \times NEX$. However, because the TRs used in GRE imaging are typ-

ically very much shorter (≈ 10 msec) than those used in SE imaging (≈ 1 sec), GRE images can be acquired in seconds rather than minutes. For example, using an image matrix of 128×128 , a TR of 10 msec, and two averages, our total image acquisition time is 2.56 sec. Because the short TRs preclude an interleaved multislice acquisition (as discussed for SE imaging), there simply is not enough time within TR for excitation and detection in other slices. Therefore, the total acquisition time for multislice imaging is

$$(\text{number of slices}) \times (\text{number of views per slice}) \times NEX \times TR. \quad (19)$$

Echo Planar Imaging Sequences

Echo planar imaging (EPI) is significantly different from standard two-dimensional Fourier transform (2DFT) imaging methods. With 2DFT methods, only one projection (or line in k -space) is acquired with each TR interval, so image acquisition time is relatively lengthy. In contrast, the EPI method acquires k -space lines needed to create an image after a single RF excitation (hence, one "plane" is acquired with one RF excitation and subsequent "echo"). First, as in a 2DFT SE sequence, a spin echo is produced by application of a 90° and a 180° RF pulse, with the echo peaking at the echo time (TE). However, rather than apply a single phase encoding gradient and a constant frequency encoding gradient, we rapidly oscillate the frequency encoding gradient during the build-up and decay of the spin echo. A series of gradient echoes is thereby produced, each one of which is separately phase encoded by application of a brief phase encoding gradient pulse. Because all of the data are acquired after a single RF pulse, the images are free from T1 weighting and can be strongly T2 weighted, with the degree of T2 weighting dependent on the value of TE.

In addition to spin-echo EPI images, it is possible to obtain gradient-echo EPI images. The acquisition method is similar to that for spin-echo EPI, except that the series of separately phase encoded gradient echoes is acquired under the envelope of a gradient-echo signal produced by a single RF pulse. The measuring time of EPI methods lies in the range of 32–128 msec. Echo planar imaging requires special hardware to allow for rapid gradient switching, whereas gradient-echo techniques can be readily implemented on standard imaging systems.

Functional MRI

The use of fMRI has grown explosively since its inception [11–15]. Among the reasons for this explosive growth are the noninvasiveness of fMRI, the wide availability of

MR scanners capable of fMRI, and the relative robustness and reproducibility of fMRI results. With these reasons for using fMRI came a proportional need for caution. The technology can be easily misused and results can be over-interpreted. A solid understanding of the basics of fMRI is necessary. In this section, we clarify these basic concepts, discuss several practical issues related to fMRI's use, and suggest potential innovations.

MAGNETIC SUSCEPTIBILITY CONTRAST

Magnetic resonance imaging emerged in the 1970s and 1980s as a method by which high-resolution anatomical images of the human brain and other organs could be obtained noninvasively [1; 16–19]. The first types of image contrast used in MRI were proton density spin–lattice relaxation (T1) and spin–spin relaxation (T2) contrast [20–24]. The many degrees of freedom in MR parameter space has allowed MR contrast types to expand from physical to physiological [25]. The types of intrinsic MRI physiological contrast that have been discovered and developed include blood flow [25–28], diffusion [25; 29–33], perfusion [25; 31–40], and magnetization transfer [25; 41; 42]. Chemical shift imaging has been able to provide information about relative concentrations and distributions of several chemical species [25; 43; 44].

The effects of endogenous and exogenous paramagnetic materials and, more generally, of materials having different susceptibilities have also been characterized. An understanding of susceptibility contrast is an essential prerequisite to the exploration of fMRI contrast mechanisms.

Magnetic susceptibility, χ , is the proportionality constant between the strength of the applied magnetic field and the resultant magnetization established within the material [45]. In most biological materials, the paired electron spins interact weakly with the externally applied magnetic field, resulting in a small induced magnetization – oriented opposite to the applied magnetic field – that causes a reduction of field strength inside the material. These materials are *diamagnetic* and have a negative magnetic susceptibility.

In materials with unpaired spins, the electron magnetic dipoles tend to align parallel to the applied field. If the unpaired spins are in sufficient concentration, this effect will dominate, causing the induced magnetization to be aligned parallel with the applied field and thus an increase in magnetic field strength inside the material. These materials are *paramagnetic*. Figure 21 illustrates magnetic field flux through diamagnetic and paramagnetic materials.

As mentioned earlier in this chapter, the Larmor relationship entails that spins will precess at a faster frequency when experiencing a higher magnetic field. In the presence of a magnetic field perturber with susceptibility that differs from surrounding tissue, spins will precess at different frequencies depending on their location relative to

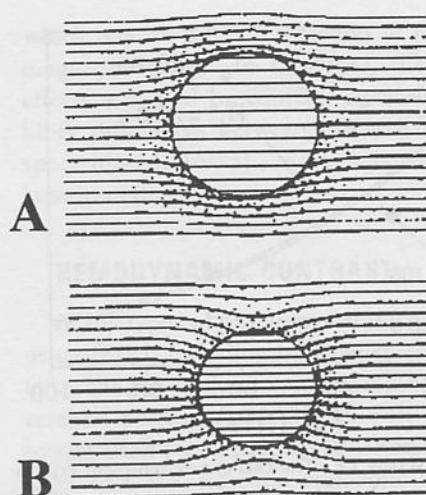


Figure 21. Illustration of the magnetic field flux through (A) diamagnetic and (B) paramagnetic materials. Within diamagnetic materials, the net flux is less; within paramagnetic materials, the net flux is greater. Magnetic field distortions created around the material are proportional to the object geometry and the difference in susceptibility between the object and its surroundings.

the perturber. In this case, the spins will rapidly become out of phase and the MRI signal will therefore be decreased. When the susceptibility differences between the perturber and its surroundings are large, the field distortions are large. Conversely, field distortions decrease when the susceptibility of the perturber becomes more similar to its surroundings; this causes more protons to have similar precession frequencies, allowing them to stay in phase longer. Increased phase coherence increases the MRI signal by decreasing the $T2^*$ and T2 decay rate. As an example, Figure 22 shows two plots of MRI signal intensity based on the simplified gradient–echo signal intensity relationship $S(TE) = S_0 e^{-TE/T2^*}$, where $S(TE)$ is the signal as a function of echo time. The signal is usually described as decaying in an exponential manner; $T2^*$ is the signal decay rate. In Figure 22, the $T2^*$ values used are 48 msec and 50 msec, and $R2^* = 1/T2^*$ (the relaxation rate).

If the signal decay over time is described as an exponential, then the natural log (Ln) of that signal will produce a straight line when plotted against time. This makes the slope more readily measurable. The slope of such a curve is simply the value $1/T2^*$ (i.e., the relaxation rate $R2^*$). Given

$$\text{Ln}(S) = TE/T2^*, \quad (20)$$

$$\text{Ln}(S)/TE = 1/T2^* = R2^*, \quad (21)$$

it follows that $R2^*$ may be obtained from the slope of $\text{Ln}(S)$ versus TE, as shown in Figure 23.

If we assume that signal changes are affected by changes *only* in $R2^*$, then the change in relaxation rate ($\Delta R2^*$) may be estimated by measuring S_r (signal during rest) and S_a (signal during activation), using only one TE value and the expression

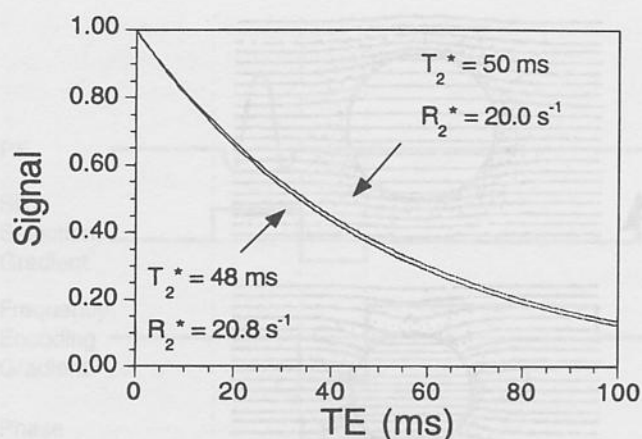


Figure 22. Plot of signal versus TE. The two curves represent typical values of R_2^* in the brain. The difference in relaxation rates represent typical differences between resting (20.8 sec^{-1}) and activated (20.0 sec^{-1}) R_2^* in the brain (-0.8 sec^{-1}). These signals are referred to as S_r (resting signal) and S_a (active signal) in the text (in general, the MR signal is denoted S).

$$\frac{-\ln(S_a/S_r)}{\text{TE}} = \Delta R_2^*. \quad (22)$$

The expression relating percent change to ΔR_2^* is

$$\text{percent signal change} = 100(e^{-\Delta R_2^*(\text{TE})} - 1). \quad (23)$$

Figure 24 is a plot of the percent signal change versus TE between the synthesized resting and activated curves. An approximately linear fractional signal increase with TE is apparent. As TE is increased, the fractional signal change increases. However, as we will show, the contrast (what really matters in an fMRI experiment) has a peak at one specific TE value.

If ΔR_2^* is small relative to R_2^* , then the signal difference between the two curves will be maximized at $\text{TE} \approx T_2^*$ (typically shorter and measured by gradient-echo pulse

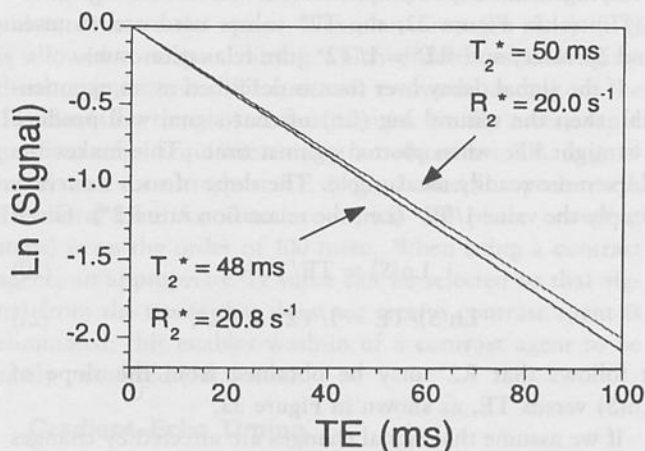


Figure 23. $\ln(S)$ versus TE. Transverse relaxation rates (R_2 and R_2^*) are measured by applying a linear fit to curves such as these. Here, activation-induced changes in S_0 are considered zero and single exponential decays are assumed.

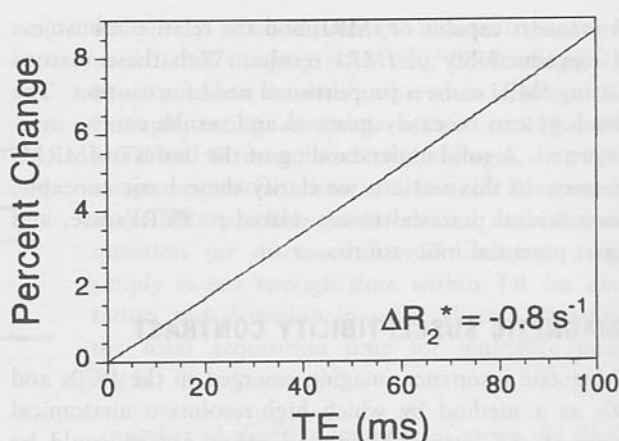


Figure 24. Percent change versus TE from the synthesized data set (see text). Given a ΔR_2^* value typically obtained, a linear dependence of percent change on TE is observed in the TE range typically used.

sequences) or T_2 (typically longer and measured by spin-echo pulse sequences), as demonstrated in what follows. The contrast between the two signal intensities (S_a and S_r) with a difference in relaxation rate of ΔR_2^* can be approximated by

$$S_a - S_r = \exp\{-\text{TE}(\Delta R_2^* + R_{2r}^*)\} - \exp\{-\text{TE}(R_{2r}^*)\}, \quad (24)$$

where R_{2r}^* is the relaxation rate associated with a measured S_r at a given TE value. The TE value at which equation (24) is maximized is given by

$$\text{TE} = \frac{\ln((\Delta R_2^* + R_{2r}^*)/R_{2r}^*)}{\Delta R_2^*}. \quad (25)$$

In the limit as ΔR_2^* approaches 0, the TE value at which contrast is maximized approaches $1/R_{2r}^*$ or T_{2r}^* . A graphical demonstration of this contrast maximization is shown in Figure 25. Even though the percent change increases, as shown in Figure 24, the contrast or signal difference does not increase monotonically with TE.

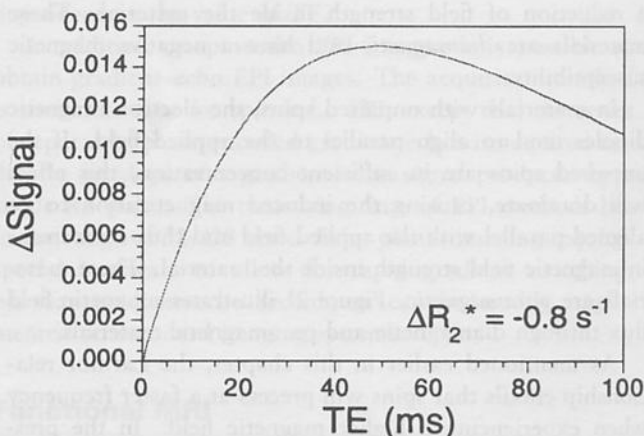


Figure 25. Plot of ΔS versus TE from the same synthesized data sets shown in the previous figures. A maximum is reached at $\text{TE} \approx T_2^*$ (approximately 48 msec).

Bulk susceptibility changes (either endogenous or exogenous) lead to MRI signal changes primarily in the manner just described. A more detailed description of the precise effects of susceptibility perturbors will be provided later.

Endogenous Susceptibility Contrast

One of the three fMRI contrast mechanisms described in this section (blood oxygenation level-dependent contrast, BOLD) is based on the understanding that blood has oxygenation-sensitive paramagnetic characteristics [45–48]. Hemoglobin is the primary carrier of oxygen in the blood. Hemoglobin that is not bound to oxygen, called deoxyhemoglobin (deoxy-Hb), contains paramagnetic iron; hemoglobin that is carrying oxygen, called oxyhemoglobin (oxy-Hb), contains diamagnetic oxygen-bound iron [45–48]. The modulation in the magnetic susceptibility of blood by changes in oxygenation is the basis of BOLD contrast. Using MR susceptometry [49], the susceptibility of completely oxygenated red blood cells was measured to be $-0.26 \pm 0.07 \times 10^{-6}$ (cgs units). With this technique, blood susceptibility was also shown to be linearly proportional to blood oxygenation (it decreases linearly as oxygenation increases). The susceptibility of completely deoxygenated red blood cells is $0.157 \pm 0.07 \times 10^{-6}$, so the susceptibility difference between completely oxygenated and completely deoxygenated red blood cells is therefore 0.18×10^{-6} . The profound effects of blood oxygenation changes on MR signal intensity have been demonstrated since 1979 [47–58].

Exogenous Susceptibility Contrast

Exogenous paramagnetic substances, which include both Gd(DTPA) and Dy(DTPA), can give useful information regarding several aspects of organ function [59]. When injected into the brain, these intravascular agents can give information on blood volume and vascular patency [49; 58–65]. The effects of these agents on tissue T1, T2*, and T2 are highly dependent on chemical environment and compartmentalization, as has been observed [49; 58–65] and modeled [59; 61–64; 66–79].

One mechanism of action for these compounds is dipolar interaction, which has an effect on intrinsic T1 and T2 relaxation times [59; 61]. This effect relies on the direct interaction of water with unpaired spins. Homogeneous distributions of solutions containing paramagnetic ions display relaxivity changes that can be predicted by the classical Solomon-Bloembergen equations [61], but in the healthy brain these injected agents remain compartmentalized within the intravascular space, which contains only about 5% of total brain water. The extent of agent-proton interaction is reduced by the limited rate at which diffusing or exchanging protons in the other 95% of brain water pass through the intravascular space, which is also less accessible owing to the blood-brain barrier. These combined effects greatly limit the agent-induced T1 effects,

which rely on direct interaction of protons with the paramagnetic agents. In this case, T2* and T2 shortening effects – caused by contrast agent-induced bulk susceptibility differences between intravascular and extravascular space [61–64; 66–75] – dominate over classical dipolar relaxation effects.

HEMODYNAMIC CONTRAST

Many types of physiological information can be mapped using fMRI, including baseline cerebral blood volume [25; 62], changes in blood volume [11], baseline and changes in cerebral perfusion [35; 38; 80–84], and changes in blood oxygenation [12; 13; 15; 85–88]. Recently, quantitative measures of CMR (cerebral metabolic rate) O₂ changes with activation have been derived from fMRI data [89–91].

Blood Volume

A technique developed by Belliveau and Rosen et al. [62; 64; 92] utilizes the susceptibility contrast produced by intravascular paramagnetic contrast agents and the high-speed capabilities of echo planar imaging (EPI) to create maps of human cerebral blood volume (CBV). A bolus of paramagnetic contrast agent is injected (the technique is slightly invasive), and T2- or T2*-weighted images are obtained at the rate of about one image per second using echo planar imaging [39; 93–95]. As the contrast agent passes through the microvasculature, magnetic field distortions are produced. These gradients (which last the amount of time that it takes for the bolus to pass through the cerebral vasculature) cause intravoxel dephasing, resulting in a signal attenuation that is linearly proportional to the concentration of contrast agent [62; 64; 76], which, in turn, is a function of blood volume.

Changes in blood volume that occur during hemodynamic stress or during brain activation can then be visualized by “subtracting” the maps imaged during a resting state from one imaged during hemodynamic stress or neuronal activation [11]. The use of this method marked the first time that hemodynamic changes accompanying human brain activation were mapped with MRI.

Blood Perfusion

An array of techniques now exist for mapping cerebral blood perfusion in humans. The MRI techniques are similar to those applied in other modalities such as positron emission tomography (PET) and single photon emission computed tomography (SPECT) in that they all involve arterial spin labeling. The MRI-based techniques hold considerable promise of high spatial resolution without the requirement of contrast agent injections. They use the fundamental idea of magnetically tagging arterial blood outside the imaging plane and then allowing flow of the tagged blood into the imaging plane. The RF tagging pulse is usually a 180° pulse that “inverts” the magnetization.

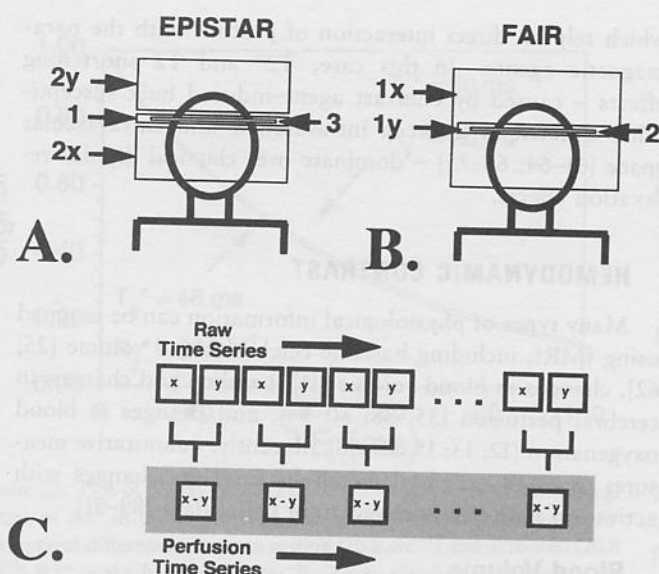


Figure 26. (A) Schematic illustration of EPISTAR (echo planar imaging with signal targeting and alternating RF). First, the imaging slice is presaturated with a saturation pulse (1). Second, protons above the imaging plane and below the imaging plane are alternately inverted or tagged (2x and 2y). Third, the image is collected after a delay time, TI, to allow the tagged protons to perfuse into the imaging plane (3). Alternate images collected in the sequential time series correspond to either the tag below (2x) or above (2y) the plane. (B) Schematic illustration of FAIR (flow-sensitive alternating inversion recovery). First, protons either within the plane or everywhere are alternately inverted or tagged (1x and 1y). Second, the image is collected after a delay time, TI, to allow the tagged protons (1x) to perfuse into the imaging plane. Alternate images collected in the sequential time series correspond to either the tag everywhere (1x) or only within (1y) the imaging plane. (C) Method by which the time series of perfusion images is created from the pulse sequences shown in (A) and (B). The alternate images, x and y, are collected in time. These images, with different tags applied, are different only in the degree to which flowing spins contribute to the signal. Therefore, a perfusion signal-only time series of images is created by pairwise subtraction of the images.

Generally, these techniques can be subdivided into (i) those that use continuous arterial spin labeling, which involves continuously inverting blood flowing into the slice [80] and (ii) those that use pulsed arterial spin labeling, periodically inverting a block of arterial blood and measuring the arrival of that blood into the imaging slice. Examples of these techniques include:

1. echo planar imaging with signal targeting and alternating RF (EPISTAR), schematically illustrated in Figure 26(A), which involves alternately inverting slabs of magnetization above and below the imaging slice [38; 39]; and
2. flow-sensitive alternating inversion recovery (FAIR), schematically illustrated in Figure 26(B), which involves the alternation between slice-selective and non-slice-selective inversion.

The latter was introduced by Kwong et al. [81; 96; 97] and referred to as FAIR by Kim et al. [84]. More recently, a

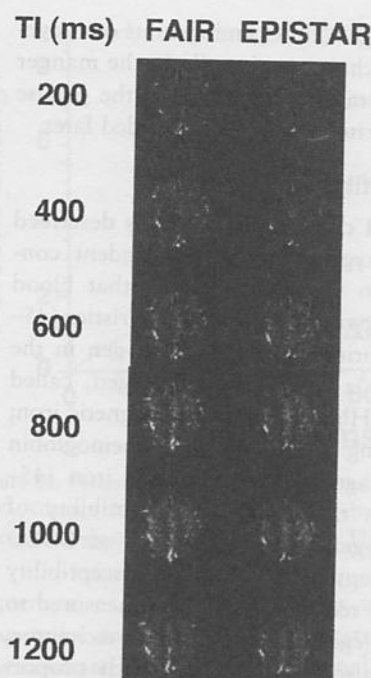


Figure 27. Comparison of EPISTAR and FAIR at corresponding TI values. As TI is lengthened, tagged blood distributes from large arteries into smaller vessels and capillary beds. In the capillaries, the tagged blood water exchanges almost completely with tissue water. Short TIs highlight rapidly flowing blood; long TIs highlight capillary bed perfusion.

pulsed arterial spin labeling technique known as QUIPSS (quantitative imaging of perfusion using a single subtraction) was introduced [83; 98]. In the case of the pulsed techniques, pairwise subtraction of sequential images – illustrated in Figure 26(C) with and without application of the RF tag outside the plane – gives a perfusion-related signal.

Varying the delay time between the inversion or tag outside the imaging plane and the acquisition of the image yields perfusion maps that highlight blood at different stages of its delivery into the imaging slice. Because there is necessarily a gap between the proximal tagging region and the imaging slice, there is a delay in the time for tagged blood to reach the arterial tree. This delay time can be highly variable, ranging from about 200 msec to about 1 sec for a gap of 1 cm. At 400 msec, typically only blood in larger arteries has reached the slice and so the pulsed arterial spin labeling signal is dominated by focal signals in these vessels; whereas at 1,000 msec, tagged blood has typically begun to distribute into the capillary beds of the tissue in the slice. Images acquired at late inversion times can be considered qualitative maps of perfusion. Figure 27 shows perfusion maps created at different TI times using both the FAIR and the EPISTAR technique. As TI is lengthened, tagged blood distributes from large arteries into smaller vessels and capillary beds. In the capillaries, the tagged blood water exchanges almost completely with

tissue water. To quantify perfusion using these techniques, it is necessary to more carefully model the phenomena and relevant variables [84; 97; 99; 100]. For quantification, a minimum of two subtractions at different TIs is required in order to calculate the rate of entry (perfusion) of tagged blood into the slice [100].

For the mapping of human brain activation (i.e., to observe only activation-induced *changes* in blood perfusion), a more commonly used flow-sensitive method is performed by applying the inversion pulse always in the same plane. In this case, the intensity of all images obtained will be weighted by modulation of longitudinal magnetization by flowing blood and also by other MR parameters that normally contribute to image intensity and contrast (proton density, T1, T2). Therefore, this technique allows only for observation of changes in flow that occur over time with brain activation. This technique was first implemented by Kwong et al. [13] to observe activation-induced flow changes in the human brain. In this seminal paper, activation-induced signal changes associated with local changes in blood oxygenation were also observed.

Blood Oxygenation

In 1990, work of Ogawa et al. [85; 101; 102] and Turner et al. [86] demonstrated that MR signals in the vicinity of vessels and in perfused brain tissue decreased with a decrease in blood oxygenation. This type of physiological contrast was coined "blood oxygenation level dependent" (BOLD) contrast by Ogawa et al. [85].

The use of BOLD contrast for the observation of brain activation was first demonstrated in August 1991 at the 10th Annual Society of Magnetic Resonance in Medicine meeting [103]. The first papers demonstrating the technique, published in July 1992, reported human brain activation in the primary visual cortex [13; 14] and motor cortex [12; 13]. Two [12; 13] of the first three reports of this technique involved the use of single-shot EPI at 1.5 Tesla. The other [14] involved multishot FLASH imaging at 4 Tesla. Generally, a small local signal increase in activated cortical regions was observed using gradient-echo pulse sequences – which are maximally sensitive to changes in the homogeneity of the main magnetic field.

The working model constructed to explain these observations with susceptibility contrast imaging is that an increase in neuronal activity causes local vasodilation, which in turn causes an increase in blood flow. This results in an excess of oxygenated hemoglobin beyond the metabolic need, thus *reducing* the proportion of paramagnetic deoxyhemoglobin in the vasculature. This hemodynamic phenomenon was previously suggested by non-MRI techniques [104–106]. A reduction in deoxyhemoglobin in the vasculature causes a reduction in magnetic susceptibility differences in the vicinity of venules, veins, and red blood cells within veins, thereby causing an increase in spin

coherence (increase in T2 and T2*) and thus an increase in signal for T2*- and T2-weighted sequences.

Presently, the most widely used fMRI technique for the noninvasive mapping of human brain activity is gradient-echo imaging using BOLD contrast. There are several reasons for this. (a) Gradient-echo T2*-sensitive techniques have demonstrated higher activation-induced signal change contrast (by a factor of 2 to 4) than T2-weighted, flow-sensitive, or blood volume-sensitive techniques. (b) The BOLD contrast can be obtained using more widely available high-speed multishot non-EPI techniques. (c) The T2*-weighted techniques are sensitive to blood oxygenation changes in vascular structures, including large vessels that may be spatially removed from the focus of activation. For most applications, techniques that are more sensitive to microvascular structures entail a too severely compromised ratio of functional contrast to noise. This last issue will be further discussed shortly.

Figure 28 gives a summary of the cascade of hemodynamic events that occur on brain activation and of their effects on the appropriately weighted MRI signal.

ISSUES IN fMRI

Although rapid progress continues, many issues in fMRI remain incompletely understood. Here we provide a description of the current state of understanding regarding some general fMRI issues, grouped under headings of interpretability, temporal resolution, spatial resolution, dynamic range, and sensitivity.

Interpretability

The question of interpretability regards the concern of exactly what the relationship is between the fMRI signal and underlying neuronal activation. Two "filters" separate direct observation of neuronal processes using fMRI. The first is the relationship between neuronal activation and hemodynamic changes, and the second is the relationship between hemodynamic changes and MR signal changes.

In the past five years, considerable progress has been made in the characterization of the second relationship: that between activation-induced hemodynamic changes and the fMRI signal changes. Here we discuss the issue of MRI-achievable hemodynamic specificity, as well as the dynamic range and the upper limits of temporal and spatial resolution of fMRI.

A high priority in fMRI is to correlate accurately the activation-induced MR signal changes with underlying neuronal processes. It is generally accepted that perfusion and oxygenation changes in capillaries are closer in both space and time to neuronal activation than changes arising in arteries or veins. As mentioned, different pulse sequences can be made sensitive to specific populations of vessel sizes, blood flow velocities, and contrast mechanisms.

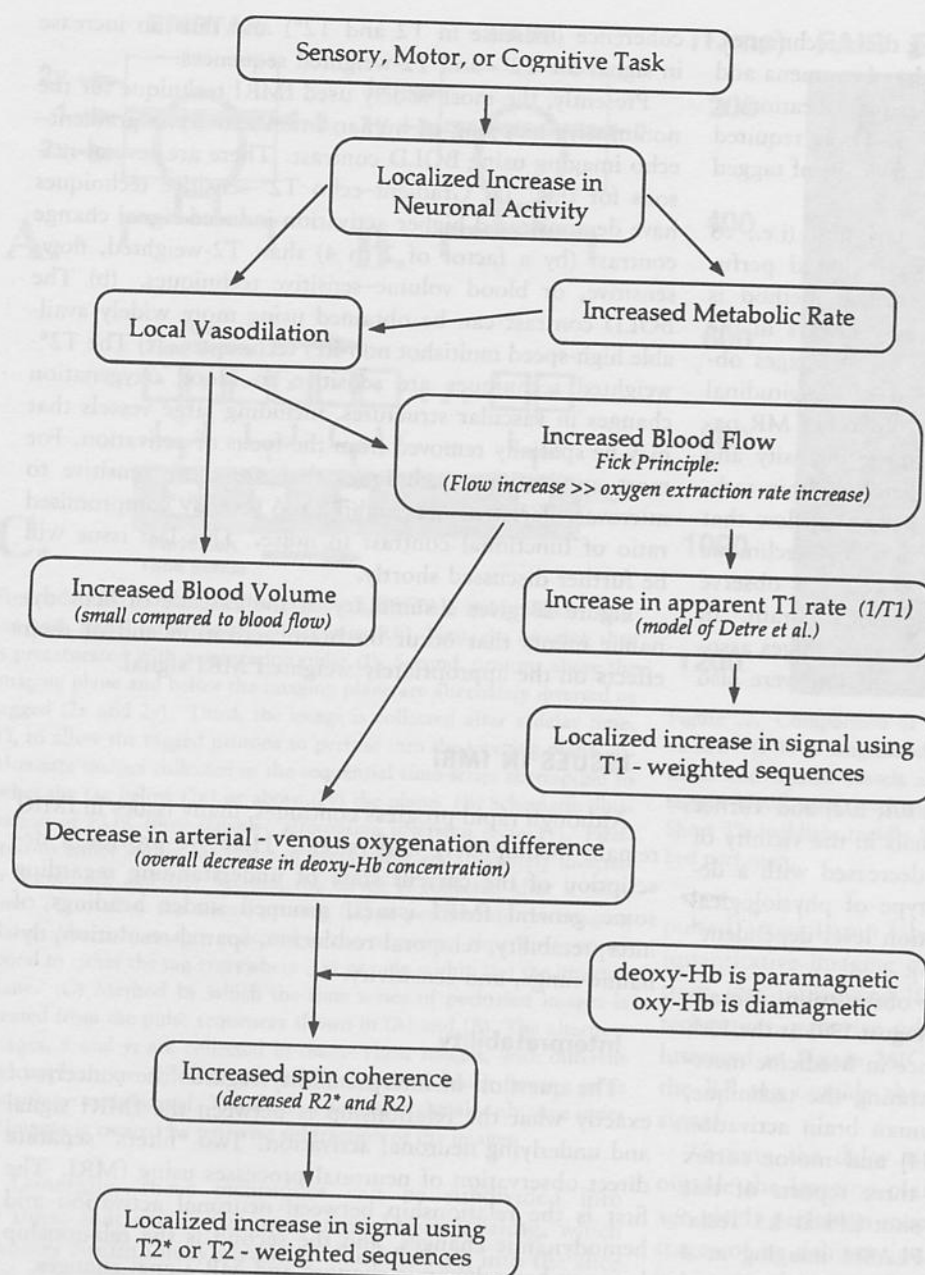
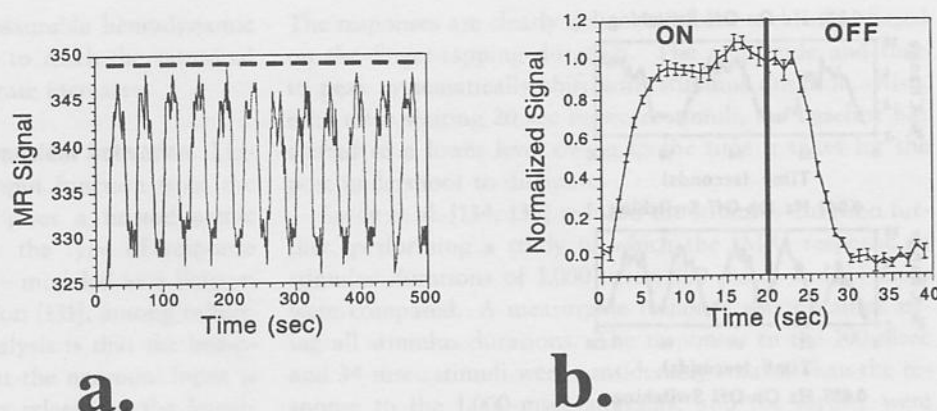


Figure 28. Flow chart summarizing the cascade of hemodynamic events that occur with brain activation and their corresponding effects on the appropriately sensitized MRI signal.

The fMRI pulse sequence that gives the highest functional contrast-to-noise ratio is a T2*-weighted gradient-echo sequence, which is likely to have contrast weighting that includes large draining vein effects and, in the case of short-TR-high flip-angle sequences (short TR values are required for non-EPI fMRI sequences), large vessel arterial inflow effects. Sequences that may be able to more selectively observe capillary oxygenation (spin-echo with velocity nulling) or perfusion (arterial spin labeling with velocity nulling) effects are less robust. They have a lower functional contrast-to-noise ratio, are generally less time-efficient, and may not allow extensive

multislice imaging. The tremendous need for high fMRI contrast-to-noise ratio, high image acquisition speed, and flexibility (e.g., multislice imaging) has to date outweighed the need, in most cases, for selective observation of capillary effects. Enhancements in fMRI sensitivity may allow these hemodynamically selective pulse sequences to be more commonly used. The strategies for achieving hemodynamic specificity include not only pulse sequence modifications but also simple vein and artery identification strategies or even activation strategies that remove draining vein effects. For a review of these sequences, see [107].



Temporal Resolution

The temporal resolution of fMRI has been variably defined in the literature. These definitions include the image acquisition rate, the time it takes for the activation-induced response to rise or fall a given amount (otherwise known as the time constant of the measured changes), the maximum rate at which activation can be turned on and off and still generate a detectable response, the smallest detectable activation duration, the smallest detectable difference in latency (between two identical activations that have different onset times) in an individual voxel or region of interest (ROI), and the smallest detectable difference in latency across separate voxels or ROIs. These aspects of fMRI temporal resolution will be discussed next.

Image Acquisition Rate. The rate at which images are acquired is determined by the pulse sequence used. Multishot functional imaging techniques do not generally require specialized gradient hardware, but they usually require at least 3 sec for image acquisition [14; 108–111]. A faster technique, single-shot echo planar imaging [94; 95; 112], generally requires specialized gradients or gradient switching hardware. The readout window width of an echo planar image is about 20–40 msec. Hybrid techniques, such as multishot EPI [113; 114], provide a good compromise in spatial resolution and time but suffer from the shot-to-shot instability characteristic of all multishot techniques. These instabilities, caused primarily by respiration and cardiac cycle effects, are reduced by spiral scanning strategies [110; 111], retrospective *k*-space realignment techniques [115], and navigator pulses [116].

In the context of fMRI, a TE in the range of 30–60 msec is optimal ($\approx T2^*$ of gray matter from 4 Tesla to 1.5 Tesla, respectively); the minimum time between successive image acquisitions (TR) is typically about 100 msec. With the use of partial *k*-space acquisition techniques and a shorter (and hence nonoptimal) TE, image acquisition rates as high as 60 images per second have been reported [117]. Issues regarding the trade-offs between image acquisition rate and functional contrast have not yet been fully resolved. From a practical standpoint, collection of a mul-

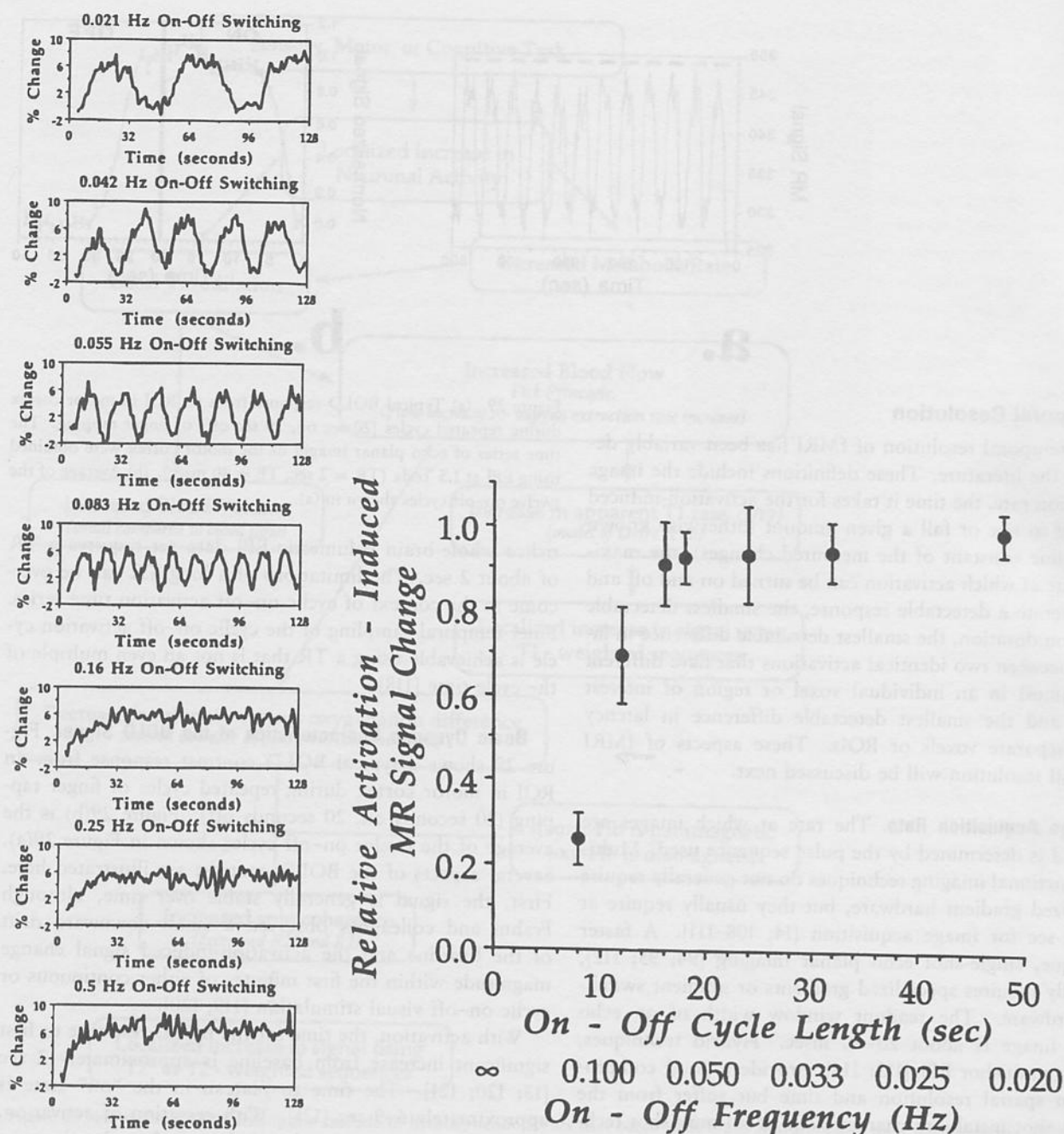
Figure 29. (a) Typical BOLD response from an ROI in motor cortex during repeated cycles (20 sec on, 20 sec off) of finger tapping. The time series of echo planar images of the motor cortex were obtained using EPI at 1.5 Tesla (TR = 2 sec, TE = 40 msec). (b) Average of the twelve on-off cycles shown in (a).

tislice whole-brain volumetric EPI data set requires a TR of about 2 sec. The limitations of a long TR can be overcome in the context of cyclic on-off activation time series. Finer temporal sampling of the cyclic on-off activation cycle is achievable using a TR that is not an even multiple of the cycle time [118].

Basic Dynamic Characteristics of the BOLD Signal. Figure 29 shows a typical BOLD contrast response from an ROI in motor cortex during repeated cycles of finger tapping (20 seconds on, 20 seconds off). Figure 29(b) is the average of the twelve on-off cycles shown in Figure 29(a). Several aspects of the BOLD contrast are illustrated here. First, the signal is generally stable over time, although Frahm and colleagues observed a small downward drift of the baseline and the activation-induced signal change magnitude within the first minutes of either continuous or cyclic on-off visual stimulation [119; 120].

With activation, the time for the BOLD response to first significant increase from baseline is approximately 2 sec [13; 120; 121]. The time to plateau in the “on” state is approximately 6–9 sec [121]. With cessation of activation, the time to return to baseline is longer than the rise time by about one or two seconds [122]. As mentioned, several groups have reported a “pre-undershoot” or initial dip during the first 500 msec [123] to 2 sec of the signal [124; 125]. More commonly observed is a post-undershoot, which is observed more in the visual than motor cortex and has an amplitude that is dependent on stimulus duration [126]. On cessation of activation, the post-undershoot signal can take up to a minute to return to baseline [120; 127].

The hemodynamic response can be thought of as a low-pass filter [128]. A straightforward method of determining the filter characteristics is to modulate the input and observe the output. Figure 30 demonstrates the effect of modulating the on-off motor cortex activation rate



a.

b.

Figure 30. (a) Signal from an ROI in motor cortex obtained during cyclic on-off finger movement. As the on-off frequency is increased from 0.021 Hz to 0.5 Hz, the activation-induced amplitude becomes decreased and the signal becomes saturated in the "on" state. (b) Summary of the dependence of the relative amplitudes of the activation-induced signal on switching frequency shown in (a). The relative signal change amplitude is reduced at on-off rates above 0.06 Hz.

from 24 sec on and 24 sec off to 1 sec on and 1 sec off. Because the time to reach a baseline after cessation of activity is slightly longer than the time to plateau in an "on" state, the signal becomes saturated in that state with the faster on-off frequencies. The relative activation-induced signal

amplitude in the motor cortex does not show a significant decrease until the switching frequency is higher than 0.06 Hz (8 sec on and 8 sec off), and it does not follow the activation timing above 0.13 Hz. Other work has shown that, with sufficient averaging, a constant on-off rate of 2 sec

on and 2 sec off can induce a measurable hemodynamic response [129; 130]. Also, the time to reach the saturated "on" state decreases as the on-off rate increases.

The Hemodynamic Response to Transient Activation. Linear deconvolution of a neuronal input function from the measured hemodynamic response gives a hemodynamic "impulse response" that resembles the type of response that is induced by a brief stimulus – modeled as a Poisson function [128] and a Gamma function [131], among others. The implicit assumption in this analysis is that the hemodynamic response is linear and that the neuronal input is a binary "boxcar" function. Issues related to the linearity of the hemodynamic response become important when considering experimental design and signal interpretability issues (discussed later in this chapter). Regardless, a brief "impulse" of activation elicits a response that quite closely resembles the shape of a deconvolved neuronal "impulse response." The first event-related fMRI experiments were performed using primary visual and motor activation [122; 132–135], demonstrating the critical fact that a single transient activation (2 sec or less) can induce a measurable hemodynamic response. The general response was shown to peak at about 4–6 sec following activation and then return to baseline at about 10 sec after activation. Details of this transient activation-induced hemodynamic response are discussed next.

The Minimum Detectable Stimulus Duration. One of the first questions asked after fMRI was discovered was, "How brief of a stimulus can one give and still elicit a measurable response?" First, Blamire et al. [132] reduced a visual stimulus duration to 2 sec, successfully showing a response. Then, Bandettini et al. [122; 133] demonstrated a response to 500-msec-duration finger tapping. Figure 31 shows these early results obtained from a region in motor cortex. The time series consist of two finger-tapping durations of 5 sec, 3 sec, 2 sec, 1 sec, and 500 msec.

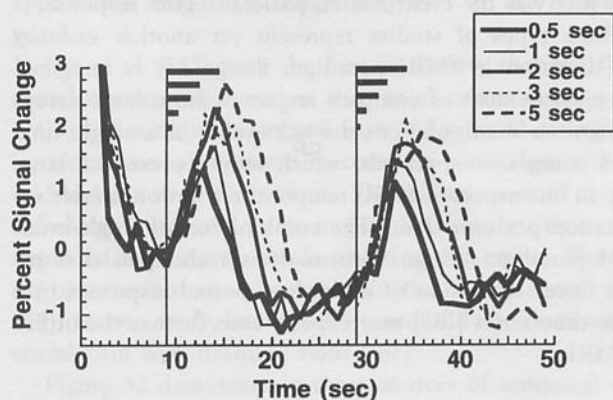


Figure 31. Signal from an ROI in motor cortex across five separate runs during which the subject was cued to perform finger tapping for 0.5, 1, 2, 3, and 5 sec twice during the time series. The time between the two finger tapping periods was 20 sec (TR = 1 sec).

The responses are clearly delineated from each other based on the finger-tapping duration. The amplitude and time to peak systematically shift with stimulus duration. Also, even after waiting 20 sec between stimuli, the baseline has shifted to a lower level owing to the time it takes for the post-undershoot to dissipate.

Savoy et al. [134; 135] reduced the stimulus duration further, performing a study in which the fMRI response to stimulus durations of 1,000 msec, 100 msec, and 34 msec were compared. A measurable response was obtained using all stimulus durations. The responses to the 100-msec and 34-msec stimuli were considerably smaller than the response to the 1,000-msec stimulus, and the former were similar in shape and amplitude to each other. These results suggest that the minimum stimulus duration has not yet been determined but that, below a specific stimulus duration, the hemodynamic response remains constant.

A Paradigm Shift in Experimental Design: Event-Related fMRI. A critical question in event-related fMRI was whether a transient cognitive activation could elicit a significant and usable fMRI signal change. In 1996, Buckner and colleagues [136] demonstrated that, in fact, event-related fMRI lent itself quite well to cognitive activation questions. In their study, a word-stem completion task was performed using a "block design" strategy and an event-related strategy. Robust activation in the regions involved with word generation were observed in both cases.

Given the substantial amount of recent publications that describe event-related fMRI [123; 129; 130; 137–154], it can probably be said that this is one of the more exciting developments in fMRI since its discovery. Several papers describing event-related signal change characteristics and analysis techniques have recently been published [95; 141; 142; 150; 151; 155; 156].

The advantages of event-related activation strategies are many [152]. These include the ability to more completely randomize task types in a time series, the ability to selectively analyze fMRI response data based on measured behavioral responses to individual trials, and the option of incorporating overt responses into a time series. Separation of motion artifact from BOLD changes is possible by the use of the temporal response differences between motion effects and the BOLD contrast-based changes [137; 157].

Experimental Design Issues in Event-Related fMRI. Experimental design and interpretation issues depend on whether the activation-induced hemodynamic response behaves like a linear system. The evidence is somewhat conflicting. Boynton et al. [150] demonstrated that, under most circumstances, the hemodynamic response behaves in a linear manner. Nevertheless, they also observed that the amplitude of the response to brief stimuli is larger than a linear system would predict. This observation was supported by Bandettini et al. [129; 130].

Reasons for nonlinearities in the event-related response can be neuronal, hemodynamic, or metabolic in nature. The neuronal input may not be a simple boxcar function. Instead, an increased neuronal firing rate at the onset of stimulation (neuronal "bursting") may cause a slightly larger amount of vasodilation that later plateaus at a lower steady-state level. The amount of neuronal bursting necessary to significantly change the hemodynamic response, assuming a linear neuronal-hemodynamic coupling, is quite large. For example, to account for the almost double functional contrast for the experimental relative to the linear convolution-derived single-event responses, the integrated neuronal response over 2 sec must double. Assuming that neuronal firing is at a higher rate for only about the first 50 msec of brain activation, the neuronal firing rate must be 40 times greater than steady state for this duration.

As is well known, BOLD contrast is highly sensitive to the interplay of blood flow, blood volume, and oxidative metabolic rate. If, with activation, any one of these variables changes with a different time constant, then the fMRI signal can show fluctuations until a steady state is reached [119; 158; 159]. For instance, an activation-induced increase in blood volume would slightly reduce the fMRI signal, since more deoxyhemoglobin would be present in the voxel. If the time constant for blood volume changes were slightly longer than that of flow changes, then the activation-induced fMRI signal would first increase and then be reduced as blood volume later increased. The same could apply if the time constant of oxidative metabolic rate were slightly slower than that of flow and volume changes. Evidence for increased oxidative metabolic rate after 2 min of activation is given by Frahm et al. [119], but no evidence suggests that the time constant of the increase in oxidative metabolic rate is only seconds longer than the flow increase time constant – as would be required for it to be applicable only to relatively high-amplitude single-event responses. These hemodynamics, which may also differ on a voxelwise basis, have yet to be characterized fully.

From this information it is clear that, when using a constant interstimulus interval (ISI), the optimal ISI is about 10–12 sec and the response is somewhat nonlinear. Nonlinearities have also been demonstrated by other studies [140; 156]. Dale and Buckner [151] have nevertheless shown that responses to visual stimuli, presented as rapidly as once every 1 sec, can be adequately separated using overlap correction or deconvolution methods. These methods are possible if the ISI is varied during the time series. Burock et al. [139] demonstrated that remarkably clean activation maps can be created using an average ISI of 500 msec and deconvolution methods to extract overlapping responses. Assuming that the hemodynamic response is essentially a linear system, there is no obvious minimum ISI; rather, there exists an optimal ISI *distribution*. An exponential

distribution of ISIs (with a mean as short as psychophysically possible) is optimal from a statistical standpoint. Of course, the rapidity with which stimuli can be presented ultimately depends on the study being performed. Many cognitive tasks may require a lower presentation rate. Several cognitive studies have been successfully performed using intermixed, rapidly presented trials [138; 149].

Although excellent activation maps can be created using rapidly presented stimuli and deconvolution methods, interpretation of details of the deconvolved responses depends on the linearity of the system. Future work in event-related experimental optimization rests in what further information can be derived from these responses. Between-region, between-voxel, between-subject, and stimulus-dependent variations in amplitude, latency, shape, and responsivity of the event-related fMRI responses are still relatively uncharacterized. Reasons for these differences are also still unclear.

Single-Event fMRI: Single-Thought Measurement. Individual responses to individual events are easily detectable even at relatively low field strengths, but it should be noted that the studies described in previous sections involved relatively long time series and considerable averaging or "binning" of the individual responses into specific categories. These approaches are extremely powerful, but repeatability of individual activation patterns is likely to be somewhat imperfect, especially across trials spaced several minutes apart.

Several studies have demonstrated the ability to create functional maps and to derive useful information using only a single response to a single input. Richter and colleagues were able to derive the relative onset of activation of supplementary motor cortex relative to primary motor cortex using a delayed motor task following a readiness cue [160; 161]. Also, Richter et al. [162] demonstrated the ability to correlate individual response widths to the duration of a mental rotation task. The larger the angle that an object was mentally rotated, the longer the task took and the wider was the event-related parietal region response.

These types of studies represent yet another exciting new direction in fMRI paradigm design. It is imagined that measurement of complex responses from large arrays of cognitive manipulations are achievable in a single time series using this approach, which may represent a large jump in one aspect of fMRI temporal resolution: usable information per unit time. The combination of single-event fMRI paradigm design with analysis techniques that involve linear regression of multiple expected responses in a single time series [163] may expand even further the utility of fMRI.

Latency Discernibility within a Voxel or Region of Interest. If a task onset or duration is modulated, such as in the aforementioned motor cortex tasks or mental rotation studies [160–162], the accuracy with which one can

temporally correlate the modulated input parameters to the measured output signal depends on the variability of the signal within a voxel or region of interest.

Savoy and colleagues [135] have addressed this issue of latency estimation accuracy. Variability of several temporal components of an activation-induced response function were determined. Six subjects were studied, and ten activation-induced response curves were analyzed for each subject. The relative onsets were determined by finding the latency with which each of the temporal "components" was maximized with each of three reference functions, representing three "components" of the response curve: the entire curve, the rising section, and the falling section. The standard deviations of the entire curve, rising phase, and falling phase were found to be 650 msec, 450 msec, and 1,250 msec, respectively. The reason for the difference between the rising phase and falling phase variability remains an open question.

Latency Discernibility across Voxels or Regions of Interest. Researchers have reported observing across-region differences in the onset and return to baseline of the BOLD signal during cognitive tasks [136; 164]. For example, during a visually presented event-related word-stem completion task, Buckner et al. [136] reported that the signal in the visual cortex increased about 1 sec before the signal in the left anterior prefrontal cortex. One might argue that this is expected, since the subject first observes the word stem and then, after about a second, generates a word to complete this task. Others would argue that the neuronal onset latencies should not be more than about 200 msec. Can inferences regarding the spatial-temporal cascade characteristics of networked brain activation be made on this time scale from fMRI data? Without controlling for the intrinsic temporal variability of the BOLD signal over space, such inferences cannot be easily made for temporal latency differences below about 4 sec. If appropriate controls are performed, then the variability approaches that of a single response in an individual voxel.

Lee et al. [165] were the first to observe that the fMRI signal change onset within the visual cortex during simple visual stimulation varied from 6 sec to 12 sec. These latencies were also shown to correlate somewhat with the underlying vascular structure. The earliest onset of the signal change appeared to be in gray matter; the latest onset appeared to occur in the largest draining veins. This basic observation was also made in the motor cortex [107; 166]. In one study, latency differences did not show a clear correlation with draining veins [167].

Figure 32 demonstrates three sources of temporal variability. Figure 32(a) shows us a plot of the average time course from the motor cortex resulting from 2-sec finger tapping. As mentioned, the first source of variability is the intrinsic noise in the time-series signal (the standard de-

viation of the signal is on the order of 1%). The second source of variability is that of the hemodynamic response, which ranges from 450 msec to 1,250 msec, depending on whether one is observing the rising or the falling phase of the signal. The third source of variability is the latency spread over space.

The plot in Figure 32(a) was used as a reference function for correlation analysis and allowed to shift ± 2 sec. Figure 32(b) is a histogram of the number of voxels in an activated region that demonstrated a maximum correlation with the reference function at each latency (relative to the average latency) to which the reference function was shifted. As can be seen, the spread in latencies is over 4 sec. Figure 32(c) includes a map of the dot product (measure of signal change magnitude) and latency, demonstrating that the regions showing the longest latency roughly correspond to the regions that show the largest signal changes. These largest signal changes are likely to be downstream draining veins.

To obtain information about relative onsets of cascaded neuronal activity from latency maps, it is important to characterize the underlying vasculature-related latency distribution at which one is looking. Savoy et al. [134; 135] demonstrated that activation onset latencies of 500 msec were discernible using a visual stimulation timing described as follows. First, the subject viewed a fixation point for 10 sec. Then, the subject's left visual hemifield was activated 500 msec before the right; both hemifields were activated for 9 sec, and then the left hemifield stimulus was turned off 500 msec before the right.

With careful choice of ROI from which the time-course plot is made, these onset differences can be shown. However, maps of latency cannot reveal the onset differences because, as mentioned, the variability over space (about 4 sec) dominates the inserted 500-msec variability from left to right hemifield. In addition, the onset latency – as derived from a time course obtained from a region of interest – is extremely sensitive to the choice of ROI, since the spatial variability is so extreme.

Modulation of the stimulation timing has allowed *relative* latency differences to be mapped. In the study shown, the left-right onset order was switched so that, in the first run, the left hemifield was activated and turned off 500 msec and 250 msec prior to the right; in the second run, the right hemifield was activated and turned off 500 msec and 250 msec prior to the left. Latency maps were made for each onset order and subtracted from each other to reveal clear delineation between right and left hemifield that was not apparent in each of the individual maps. This operation is shown in Figure 33. It should be noted that maps are of the change in onset of one area relative to another and not of absolute latency. Maps such as these may be extremely useful in determining which regions of activation are modulated relative to other areas, given a specific and measurable task timing or response variation.

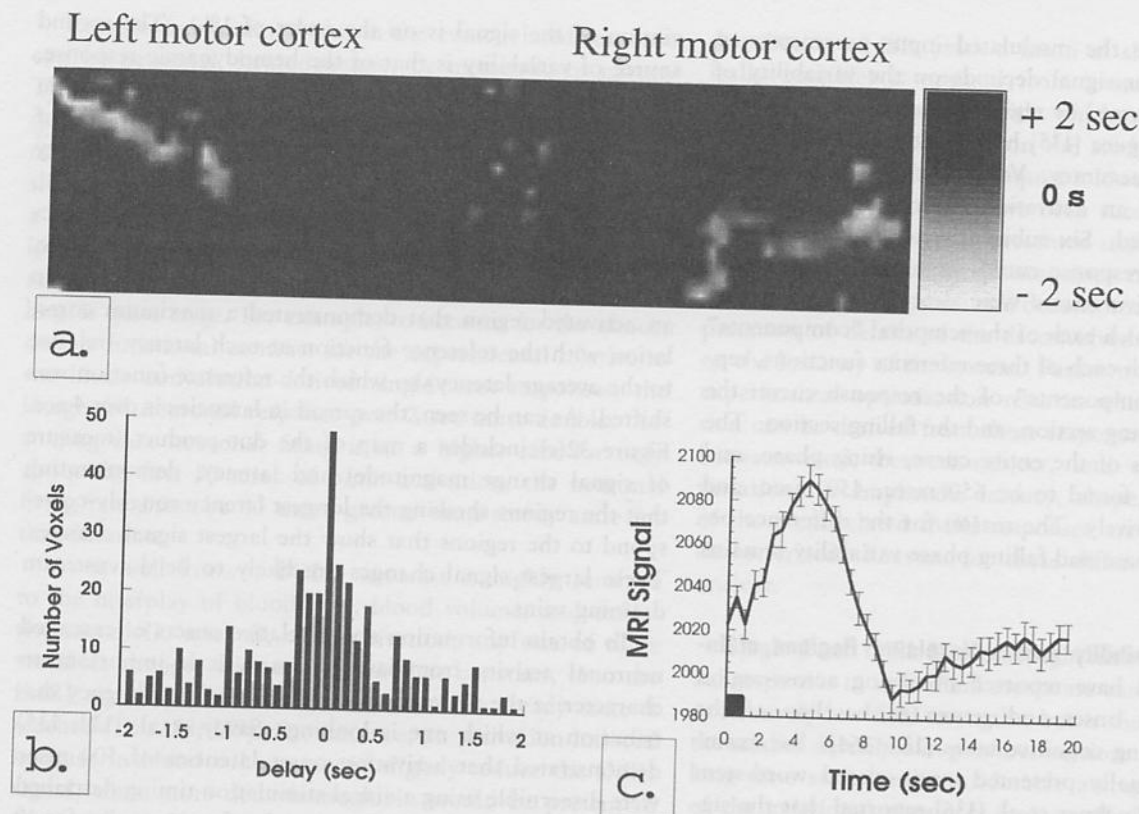


Figure 32. Demonstration of several of the limits of fMRI temporal resolution. Echo planar imaging was performed at 3 Tesla using a Bruker Biospec 3T/60 equipped with a local head gradient coil. A time-course series of axial images (matrix size = 96×96 , FOV = 20 cm, TE = 40 msec, TR = 500 msec, flip angle = 80°) through the motor cortex was obtained. Bilateral finger tapping was performed for 2 sec, alternating time and space. (a) Time course of the signal elicited by tapping fingers for 2 sec. The standard deviation of the hemodynamic change, in time, is in the range of 450–650 msec. (b) Map of the dot product (a measure of the activation-induced signal change magnitude) and the relative latencies or delays of the reference function (the plot in (a) was used as the reference function) at which the correlation coefficient was maximized. The spatial distribution of hemodynamic delays has a standard deviation of about 900 msec. The longest delays approximately match the regions that show the highest dot product and the area where veins are shown as dark lines in the T2*-weighted anatomical image. (c) Histogram of relative hemodynamic latencies; this was created from the latency map in (b).

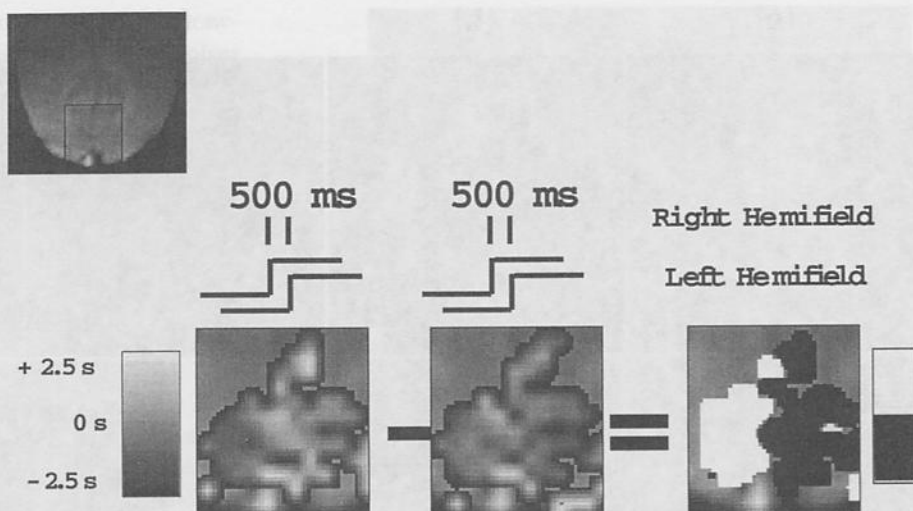
A similar study by Luknowski et al. [168] showed that the mean accuracy of latency measures from multivoxel ROIs is ± 27 msec, which is comparable to that of electrophysiological experiments.

Spatial Resolution

As with temporal resolution, the upper limit on functional spatial resolution is likely determined not by MRI limits but by the hemodynamics through which neuronal activation is transduced. Evidence from *in vivo* high-resolution optical imaging of the activation of ocular dominance columns [104; 105; 169] suggests that neuronal control of blood oxygenation occurs on a spatial scale of less than 0.5 mm. Magnetic resonance evidence suggests that the blood oxygenation increases occurring with brain activation are more extensive than the actual activated regions [165; 170–173]. In other words: it is possible that, whereas the local oxygenation may be regulated on a sub-millimeter scale, the subsequent changes in oxygenation

may occur on a larger scale owing to a spillover effect. An example of this difference in activated region is given in Figures 34 and 35.

Figure 34 shows a comparison of a spin-tagging technique (FAIR) with BOLD contrast functional imaging. Low-resolution (64×64) and high-resolution (128×128) anatomical and functional (correlation maps) BOLD contrast images (gradient-echo, TE = 40 msec) were obtained of an axial slice through the motor cortex. Single-shot EPI was performed using a local gradient coil [174] and a 3T/60 Bruker Biospec scanner. The images were 5 mm thick and the FOV was 20 cm. The task was bilateral finger tapping. Resting and active state perfusion maps, created using FAIR (TI = 1,400 msec, TR = 2 sec, spin-echo TE = 42 msec), are also shown. Functional correlation maps using BOLD contrast at the two different resolutions are compared with a functional correlation map using the FAIR perfusion time-course series. The magnified images, shown in Figure 35, illustrate that the areas of activation obtained



using FAIR and BOLD contrast generally overlap but also have some significant differences. These spatial shifts in activation are likely to be due to the differences in hemodynamic sensitizations of the two sequences. The FAIR technique using a TI of 1,400 msec is optimally sensitized to imaging capillary perfusion, as shown in the resting and active state flow maps. The BOLD contrast functional images are strongly weighted by the effects of large draining veins.

In general, achieving the goal of high-spatial resolution fMRI requires a high functional contrast to noise and reduced signal contribution from draining veins. Greater hemodynamic specificity – accomplished by proper choice of pulse sequence (selective to capillary effects), innovative activation protocol design (phase tagging), and/or proper interpretation of signal change latency (latency mapping) – may allow for greater functional spatial resolution. If the contribution to activation-induced signal changes from larger collecting veins and arteries can be easily identified and eliminated, then (i) our confidence in localization of brain activation will increase and (ii) the upper limits of spatial resolution will be determined by scanner resolution and functional contrast to noise rather than by variations in vessel architecture.

Currently, voxel volumes as low as $1.2 \mu\text{l}$ have been obtained by functional FLASH techniques at 4 Tesla [175], and experiments specifically devoted to probing the upper limits of functional spatial resolution (using spiral scan techniques) have shown that fMRI can reveal activity localized to patches of cortex having a size of about 1.35 mm [176]. These studies and others using similar methods [121; 176–179] have observed a close tracking of MR signal change along the calcarine fissure as the location of visual stimuli was varied.

The voxel dimensions typically used in single-shot EPI studies are in the range of 3–4 mm in plane, with 4–10-mm slice thicknesses. These dimensions are determined by

Figure 33. Activation within a region of visual cortex is shown for two separate conditions. In one condition (left), the right visual hemifield stimulation precedes the left by 500 msec (top) and 250 msec (bottom). In the other condition (middle), the left precedes the right by 500 msec and 250 msec. Latency maps from both of these conditions show an intrinsic spread of ± 2.5 sec, which is too large to clearly identify the relative latencies across hemifields. However, once the data are normalized for this intrinsic variance (by directly comparing the hemodynamic response from the two different lags within individual voxels), the offset between left and right hemifield can be observed (right). This demonstrates that normalization of the hemodynamic lag can allow small *relative* temporal offsets to be identified. These normalized offsets can then be compared across regions to make inferences about neuronal delay. For this experiment, the TR was 400 msec.

practical limitations such as readout window length, sampling bandwidth, S/N, limits of dB/dt , and data storage capacity. Other ways to bypass the practical scanner limits in spatial resolution include partial k -space acquisition [95] and multishot mosaic or interleaved EPI [95; 113; 114]. In many fMRI situations, multishot EPI may be the optimum compromise between spatial resolution, S/N, and temporal resolution for fMRI.

Dynamic Range

It is important not to interpret spatial differences in fMRI signal change magnitude as indications of differences in the degree of neuronal activation, because the signal is highly weighted by hemodynamic factors such as the distribution of blood volume across voxels. Nonetheless, it is possible to observe differences in fMRI signal change in the same regions but across incrementally modulated tasks. This may be a useful method for extracting more direct neuronal information from the fMRI time-course series.

The first demonstration that fMRI response is not simply binary was made by Kwong et al. [13]. Both flow- and oxygenation-sensitized MR signal in V1 were measured as flicker rate was modulated. The signal behavior corresponded closely with that obtained with a previous

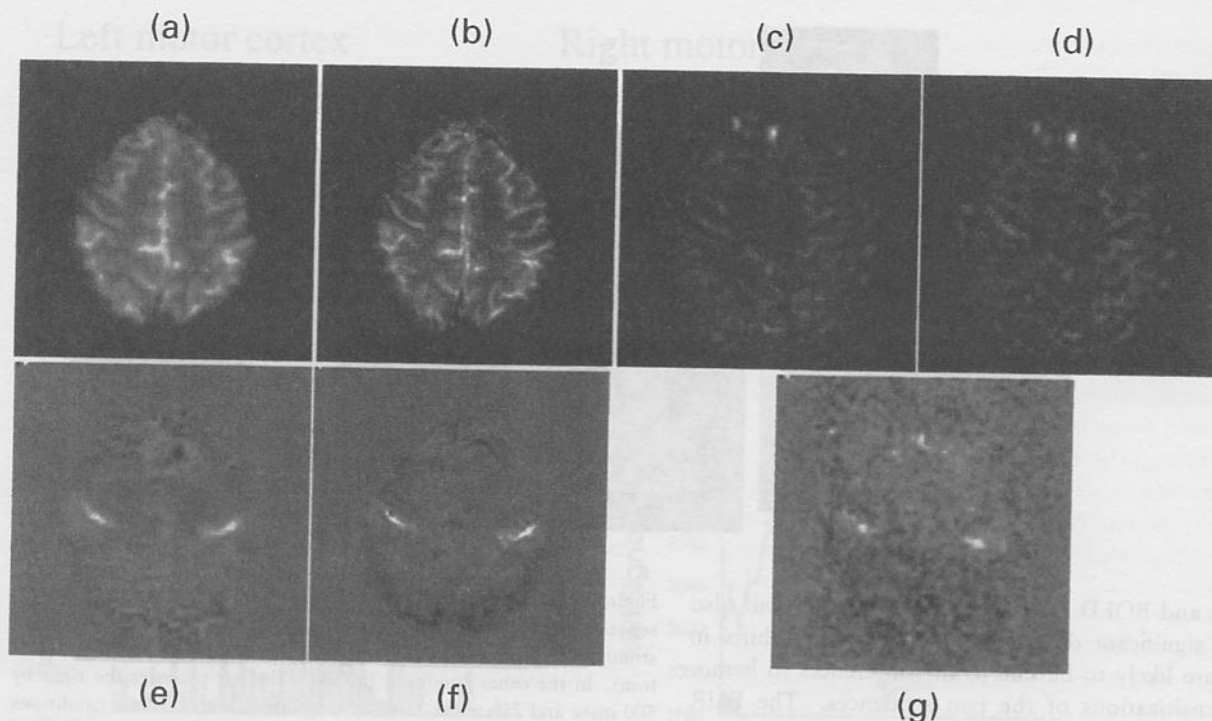


Figure 34. Comparison of perfusion-weighted and BOLD-weighted functional echo planar images at 3 Tesla. Echo planar imaging was performed using a Bruker 3T/60 scanner and a local head gradient coil. All images were created of the same plane in the same experimental session. The slice thickness was 5 mm and the FOV was 20 cm. An axial plane was chosen which contained the motor cortex. (a) 64×64 gradient-echo anatomical image (TE = 50 msec, TR = ∞). (b) 96×96 gradient-echo anatomical image (TE = 50 msec, TR = ∞). (c) Perfusion image created during the resting state using a FAIR time course series (TI = 1,400 msec, spin-echo TE = 60 msec, TR = 2 sec). (d) Perfusion image created from the same time course series as (c) during bilateral finger tapping. (e) 64×64 BOLD contrast functional correlation image created from the time series of images in which image (a) was the first of the series. Bilateral finger tapping was performed. (f) 96×96 BOLD contrast functional correlation image created from the time series of images in which image (b) was the first of the series. Bilateral finger tapping was performed. (g) 64×64 perfusion-only functional correlation image created from the same time series of perfusion images from which the resting state (c) and active state (d) images were created. Note the difference in spatial location of the area of activation between the flow-weighted and perfusion-weighted functional images. The "hot spot" in the BOLD contrast images is likely to be a draining vein, which does not appear in the perfusion-weighted functional image created using FAIR.

PET study [180]. Other studies have revealed a responsiveness in higher visual areas to contrast and flicker rate [181; 182]. In the primary motor cortex, a linear signal dependence on finger tapping rate has been demonstrated [183]. In the primary auditory cortex, a sublinear dependence on syllable presentation rate has been demonstrated [184].

Sensitivity

Extraction of a 1% signal change (which is typical of fMRI) against a backdrop of motion, pulsation, and noise requires careful consideration of the variables influencing the signal detectability. These variables span factors that increase signal, increase fMRI contrast, reduce physiologic noise, and reduce artifactual signal changes. Next we present a list of some salient variables that are important to consider in relation to optimizing fMRI sensitivity.

Averaging. Averaging of sequentially obtained images increases the S/N by the square root of the number of images collected. One difficulty is that, if averaging is performed over too long a period (exceeding ≈ 5 min), then

systematic artifacts (i.e., slow movement or drift) tend to outweigh the benefits obtained from averaging for that duration.

Field Strength. As previously discussed, S/N and functional contrast increase with field strength. However, such difficulties as increased shimming problems, increased physiologic fluctuations, and limitations on the possible RF coils used also increase with field strength. It has yet to be determined if gains in sensitivity and contrast obtained by increasing field strength cannot be achieved by other methods at lower fields, or if the gains in sensitivity and contrast outweigh the disadvantages of imaging at high field strengths.

Filtering. In most fMRI studies using EPI, the noise over time is dominated not by system noise but by physiologic fluctuations. These fluctuations correspond to specific frequencies (i.e., heart and respiration rates). Filtering out of these frequencies can increase the functional contrast-to-noise ratio, or at least make the noise closer to Gaussian so that parametric statistical tests can be applied.

Gating. Gating is a technique whose one serious drawback has at least a potential solution. Gating involves triggering of the scanner to the heart beat so that an image is always collected at a specific phase of the cardiac cycle. This is advantageous because a primary source of noise is collection of images at different phases of the cardiac cycle, which causes head misregistration (the brain moves with every heartbeat) and pulsatile flow artifacts. Image collection at a single phase would eliminate this misregistration, thereby reducing the noise and potentially increasing the spatial resolution of fMRI (i.e., the brain would be imaged at a single position all of the time). The drawback to gating is that if the heart rate changes during the collection of images then the MR signal intensity also changes, depending on the tissue T1 and the average TR used. This generally causes very large fluctuations in the data – which makes gating relatively worthless in the context of fMRI. However, a technique has been developed to correct for the global fluctuations that occur with heart rate changes [185], which would make gating a feasible option in fMRI. Gating would be especially useful for identifying activation in structures at the base of the brain, since that is where pulsatile motion is greatest, where activation is most subtle, and where activated regions are the smallest – requiring the most consistent image-to-image registration.

Paradigm Timing. The choice in fMRI timing is usually determined by the sluggishness of the hemodynamic response (it is seldom useful to go much faster than an on-off cycle of 8 sec on, 8 sec off), the particular brain system that is being activated (cognitive tasks may have a more delayed response), and the predominant frequency power of the noise. As a rule of thumb, the goal is to maximize both the number of on-off cycles and the amplitude of the cycle in order to maximize the power of postprocessing techniques such as correlation analysis [186] to extract functional information. Generally, contrast-to-noise ratio is maximized and artifact is minimized by cycling the activation at the highest rate that the hemodynamics can keep up with and by having a time-course series of no longer than about 3–4 min.

Postprocessing. Many approaches have been used to extract from fMRI data estimates of the significance, amplitude, and phase of the functional response, yet there is still surprisingly little agreement on the appropriate techniques. A review has recently been published on statistical software packages for fMRI [187]. Generally speaking, if one knows the exact shape and phase of the expected signal response then a matched filter (i.e. correlation) approach may be optimal. If the shape is unknown, then use of a single expected response function (boxcar function or a sine wave) may miss unique activation patterns. The challenge of accurately determining regions of sig-

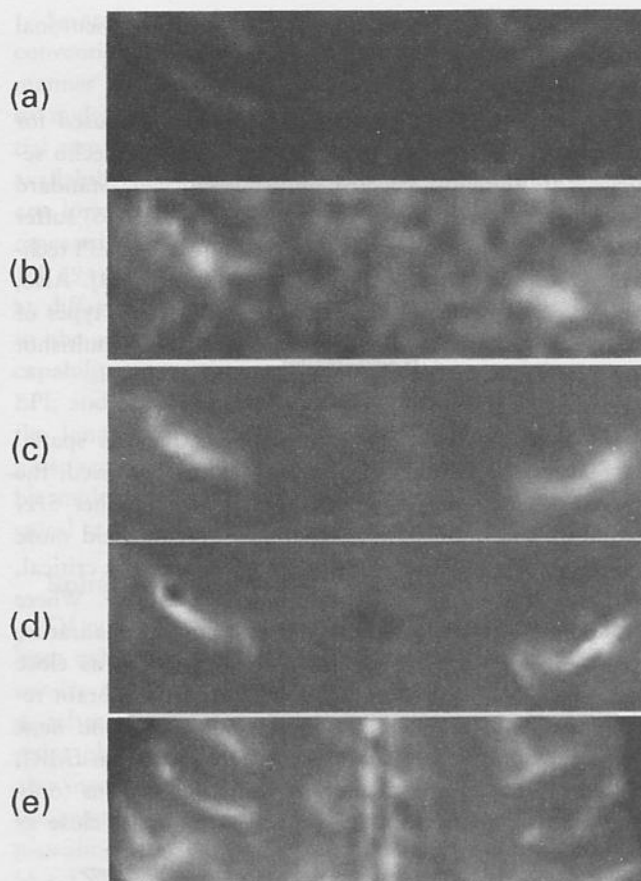


Figure 35. Magnification of selected images displayed in Figure 34 to emphasize the differences in the activation locations that appear with different hemodynamic sensitizations. (a) Baseline 64×64 perfusion image – magnification of Figure 34(c). (b) 64×64 perfusion-only-sensitive functional correlation image – magnification of 34(g). (c) 64×64 BOLD contrast functional correlation image – magnification of 34(e). (d) 96×96 BOLD contrast functional correlation image – magnification of 34(f). (e) 96×96 gradient-echo anatomical image – magnification of 34(b). Dark lines in the image are likely due to deoxygenated veins (lower T2* and phase difference from other tissue in voxel, thereby causing dephasing).

nificant activation from fMRI data is nontrivial and has yet to be solved. Some of the techniques for addressing this issue include: (a) development of accurate and robust motion correction/suppression methods; (b) determination of the noise distribution [121; 188; 189]; (c) determination of the temporal [128] and spatial [190] correlation of activation-induced MR signal changes and of baseline MR signal; (d) characterization or assessment of the temporal behavior or shape of activation-induced signal changes [121; 164; 184; 191; 192]; and (e) characterization of how the aforementioned factors vary in time and space [165; 193], across tasks [121; 191; 192], and with different pulse sequence parameters [13].

It is important always to inspect the data for motion and not to assume too much about the expected response and yet, at the same time, to use all of the current a priori

information about hemodynamic responses and neuronal activation to extract meaningful information.

Pulse Sequence. Pulse sequences that can be used for fMRI have a wide range of sensitivities; gradient-echo sequences are the most sensitive and time-efficient. Standard clinical multishot techniques (i.e., FLASH or GRASS) suffer from significantly more motion-related noise than EPI techniques or spiral multishot techniques [110; 111; 194]. Also, application of navigator echoes [110; 116] or other types of image reconstruction-related postprocessing of multishot data can significantly reduce artifactual fluctuations.

Choice of RF Coil. The trade-off here regards spatial coverage versus sensitivity. The smaller the coil used, the less brain tissue it couples to. This gives a higher S/N but much less brain coverage; larger RF coils yield more brain coverage but lower S/N. Where sensitivity is critical, a surface coil in a specific region may be desirable. Where whole-brain imaging is desirable, a whole-brain quadrature RF coil is optimal [195]. This coil is generally as close to the head as possible and couples only to the brain region. It should be noted that typical whole *head and neck* coils used clinically are suboptimal for whole-brain fMRI, since they couple also to the face and neck regions (only adding noise) and since they are generally not as close as possible to the head.

Voxel Size. The signal-to-noise ratio is directly proportional to voxel volume. Functional contrast to noise is optimized by matching the volume of the active region to the voxel volume. Because functional region sizes are not well characterized and are likely to vary widely, the optimal voxel size is difficult to predict. Many have generally matched the voxel slice to the cortical thickness. Other groups have used a slightly thicker slice to increase brain coverage given a limitation in the number of slices obtainable. As described before, spatial resolution may actually be *reduced* with the use of smaller voxels if the contrast-to-noise ratio is not high enough to detect more subtle capillary effects. In such a case of low contrast to noise, primarily downstream draining veins would be detected. This phenomenon may explain the exclusive detection of large vessels by Lai and Haacke et al. [172; 173] using small voxels. Overall, small voxels are desirable as long as the sensitivity remains high enough to detect a 1% signal change.

COMMON fMRI PLATFORMS

In an attempt to bring together much of what has been discussed so far, in this section we describe some of the most commonly used platforms for fMRI. The three types of fMRI pulse sequences examined here are EPI, conventional multishot imaging, and spiral scanning.

Echo Planar Imaging

Echo planar imaging is an ultrafast MRI technique [39; 93–95] that has been (and continues to be) ubiquitous in the ongoing development and application of fMRI. In most of the growing number of centers with EPI capability, it is the fMRI method of choice for most applications.

The EPI technique has several drawbacks (low spatial resolution, high sensitivity to off-resonance effects, need for specialized hardware, potential for peripheral nerve stimulation, and need for specialized image reconstruction algorithms). The advantages of EPI (high temporal resolution, high flexibility for imaging several types of physiological processes, high stability, low imaging duty cycle, low sensitivity to motion) still greatly outweigh the disadvantages for most purposes related to fMRI. Following is a brief description of some of these EPI characteristics.

Spatial resolution in single-shot EPI is limited either by the area of k -space that can be sampled in approximately one $T2^*$ period or by the system bandwidth [196]. The area of k -space that can be covered is limited by either the velocity in k -space (gradient amplitude) or the acceleration in k -space (gradient slew rate) – and typically by both.

The requirement with EPI for strong and rapidly switching gradients is satisfied by (1) increasing the gradient amplifier power or using a speed-up circuit; (2) implementing resonant gradient technology; (3) reducing the inductance of the gradient coils so that they can be driven by conventional gradient amplifiers; or (4) increasing the field of view and/or lowering the resolution to match the speed at which standard gradient amplifiers can keep up.

The first strategy is probably the least commonly used, whereas the second strategy is likely the most common EPI technique. Strategies (1) and (2) both use whole-body gradient coils, which allow performance of EPI for functional and/or kinematic studies on the heart, lungs, digestive system, kidneys, throat, joints, and muscles. In the context of fMRI, whole-body gradients allow more accessibility for patients with mobility problems and for easy delivery of brain activation stimuli.

The third strategy is used primarily by several centers that have home-built gradient coils. This strategy is implemented by using a gradient coil that is localized only to the head. The gradient fields are optimized for a region that usually covers the brain and/or the region of RF sensitivity. Finally, single-shot EPI can be carried out on a conventional imaging system without the use of local gradient coils (i.e., using the whole-body gradient coil) by simply using a large FOV and/or a small image matrix size [197]. Functional MRI using EPI with voxel sizes of about 10 mm × 10 mm × 10 mm (the approximate resolution of a PET scanner) have been performed on a standard GRE 1.5-Tesla Signa system with excellent results [198]. This type of echo planar imaging capability exists on practically every clinical scanner in the world.

The requirements for successful implementation of EPI for fMRI are not limited to hardware. In most cases, phase correction algorithms (applied during image reconstruction) are necessary to compensate for timing errors related to imperfections in the gradients, gradient-induced eddy currents, or static field inhomogeneities. A major non-hardware-related limitation on gradient slew rate is the biological threshold for neuronal stimulation due to time-varying magnetic fields. At present, high-performance gradient systems (either local gradient coils or high-powered whole-body systems) are capable of exceeding the FDA guidelines on gradient field slew rate (dB/dt). This is a large determinant of the upper limit on the resolution possible using single-shot EPI to image humans.

Because of the long sampling time and artifactual phase modulation, EPI is sensitive to two types of off-resonance artifacts: signal dropout and image distortion. Signal dropout is primarily due to intravoxel phase dispersion resulting from through-plane variation of magnetic field. The problem of signal dropout in gradient-echo sequences can be reduced by reduction of the TE, reduction of the voxel volume, and/or localized shimming. Also, this effect is greatly reduced in spin-echo EPI because the macroscopic off-resonance effects are refocused at the echo time.

Image distortion is caused by an off-resonance phase modulation that occurs during data acquisition. In EPI, this linear phase modulation creates a primarily linear distortion of the image in the phase encoding direction. Several postprocessing methods have been put forward for correcting image distortion in EPI [198; 199].

With the use of EPI, approximately ten images may be obtained per second – allowing the option to image the entire brain in under 2 sec or to sample a smaller number of imaging planes and so allow a more dense sampling of the time course. Another possibility in EPI is to sample less densely in space but to cover a large volume in a single shot; this technique is known as echo volume imaging (EVI) [93; 200].

A practical but significant factor to be considered when performing fMRI with EPI is the rapidity with which large amounts of data are collected. This data may then go through several additional transformations (adding to the total required data storage capacity) before a functional image is created. If 10 slices of 64×64 resolution are acquired every 2 sec. (typical for multislice fMRI), then the data acquisition rate is approximately 2 MB per minute.

Conventional Multishot Imaging

High-resolution fMRI techniques developed for use with conventional gradients include multishot FLASH [14; 108; 173; 201–204], turbo-FLASH [205], low-resolution EPI [132; 206], multishot or interleaved EPI [113; 114], echo-shifted flash [207; 208], keyhole imaging [209], and fast spin-echo [210].

Several centers have been able to successfully implement conventional multishot techniques in a routine and robust manner for fMRI [108; 172; 175; 201]. The advantages to multishot techniques are relatively high in-plane spatial resolution, less sensitivity to off-resonance effects, and availability on most clinical scanners. The disadvantages are: lower temporal resolution; increased noise due to non-repeated shot-to-shot misregistration of k -space lines [110; 111; 194] owing to variable sampling of low-frequency lines at different phases of the cardiac cycle; lower signal due to the need for short TR and low flip angles; reduced capability to perform multislice fMRI as rapidly as with EPI; and less flexibility or “dead time” (which comes with the long TR typically used for EPI) for other types of pulse sequence manipulations. More time-efficient and stable multishot techniques include fast spin-echo [210] and spiral scan imaging [110; 111; 194].

Spiral Scanning

Of non-EPI techniques, the most temporal stability has been exhibited by multishot spiral scan sequences, which involve traveling outward from the center of k -space in a spiral manner and are used in conjunction with a single-point phase correction scheme [194; 211]. Spiral scanning also involves oversampling at the center of k -space – where the acquisitions are intrinsically gradient-moment nulled – providing less sensitivity to phase errors caused by brain, blood, or cerebral spinal fluid pulsations with the cardiac cycle.

Spiral scanning has been used for many fMRI applications [176; 177; 190; 212] and has demonstrated, when used in conjunction with a phase-tagging activation scheme, the highest functional resolution (1.35 mm) to date [176]. In studies where high spatial resolution is important or where EPI is unavailable, spiral scan appears to be the method of choice.

Several review articles and chapters on fMRI techniques and applications are available [107; 122; 166; 190; 213–221].

Epilogue

Since its inception in 1991, fMRI has evolved rapidly into a highly robust and widely used technique. It is fraught with technical difficulties, most of which are fully solvable. The technique is also full of surprises and likely to have at least several uses and new directions not yet uncovered. Our hope is that the reader of this chapter will come away with a clear sense of the sophistication necessary to conduct fMRI well and with a solid understanding of successful fMRI implementation.

NOTE

This work was supported in part by grant MH51358 from the National Institutes of Health.

REFERENCES

- [1] Lauterbur, P. C. (1973). Image formation by induced local interactions: Examples employing nuclear magnetic resonance. *Nature*, 242, 190-1.
- [2] Bracewell, R. N. (1965). *The Fourier Transform and Its Applications*. New York: McGraw-Hill.
- [3] Twieg, D. B. (1983). The k -trajectory formulation of the NMR imaging process with applications in analysis and synthesis of imaging methods. *Medical Physics*, 10, 610-21.
- [4] Mezrich, R. (1995). A perspective on k -space. *Radiology*, 195, 297-315.
- [5] Ljunggren, S. (1983). A simple graphical representation of Fourier-based imaging methods. *J. Magn. Reson.*, 54, 338-43.
- [6] Hennig, J., Nauerth, A., & Friedburg, H. (1986). A fast imaging method for clinical MR. *Magn. Reson. Med.*, 3, 823-33.
- [7] Chien, D., & Edelman, R. R. (1991). Ultrafast imaging using gradient echoes. *Magn. Reson. Quart.*, 7, 31-56.
- [8] Buxton, R. B., Fisel, C. R., Chien, D., & Brady, T. J. (1989). Signal intensity in fast imaging. *J. Magn. Reson.*, 83, 576-85.
- [9] Haase, A., Frahm, J., Matthaei, D., Hanicke, W., & Merboldt, K.-D. (1986). FLASH imaging. Rapid NMR imaging using low flip-angle pulses. *J. Magn. Reson.*, 67, 258-66.
- [10] Atkinson, D. J., Burstein, D., & Edelman, R. R. (1990). First pass cardiac perfusion: Evaluation with ultrafast MR imaging. *Radiology*, 174, 757-62.
- [11] Belliveau, J. W., Kennedy, D. N., McKinsty, R. C., Buchbinder, B. R., Weisskoff, R. M., Cohen, M. S., Vevea, J. M., Brady, T. J., & Rosen, B. R. (1991). Functional mapping of the human visual cortex by magnetic resonance imaging. *Science*, 254, 716-19.
- [12] Bandettini, P. A., Wong, E. C., Hinks, R. S., Tikofsky, R. S., & Hyde, J. S. (1992). Time course EPI of human brain function during task activation. *Magn. Reson. Med.*, 25, 390-7.
- [13] Kwong, K. K., Belliveau, J. W., Chesler, D. A., Goldberg, I. E., Weisskoff, R. M., Poncelet, B. P., Kennedy, D. N., Hoppel, B. E., Cohen, M. S., Turner, R., Cheng, H. M., Brady, T. J., & Rosen, B. R. (1992). Dynamic magnetic resonance imaging of human brain activity during primary sensory stimulation. *Proc. Nat. Acad. Sci. USA*, 89, 5675-9.
- [14] Ogawa, S., Tank, D. W., Menon, R., Ellermann, J. M., Kim, S.-G., Merkle, H., & Ugurbil, K. (1992). Intrinsic signal changes accompanying sensory stimulation: Functional brain mapping with magnetic resonance imaging. *Proc. Nat. Acad. Sci. USA*, 89, 5951-5.
- [15] Frahm, J., Bruhn, H., Merboldt, K. D., Hanicke, W., & Math, D. (1992). Dynamic MR imaging of human brain oxygenation during rest and photic stimulation. *JMRI*, 2, 501-5.
- [16] Mansfield, P., & Grannell, P. K. (1973). NMR diffraction in solids? *J. Phys. C., Solid State Phys.*, L422-L426.
- [17] Mansfield, P., & Grannell, P. K. (1975). "Diffraction" and microscopy in solids and liquids by NMR. *Phys. Rev. B*, 12, 3618-34.
- [18] Mansfield, P., & Morris, P. G. (1982). *NMR Imaging in Biomedicine*. New York: Academic Press.
- [19] Morris, P. G. (1986). *Nuclear Magnetic Resonance Imaging in Medicine and Biology*. Oxford University Press.
- [20] Edelstein, W. A., Bottomly, P. A., Hart, H. R., & Smith, L. S. (1983). Signal, noise, and contrast in nuclear magnetic resonance (NMR) imaging. *J. Comput. Assist. Tomogr.*, 7, 391-401.
- [21] Young, I. R., Burl, M., & Bydder, B. M. (1986). Comparative efficiency of different pulse sequences in MR imaging. *J. Comput. Assist. Tomogr.*, 10, 271-86.
- [22] Fox, R. A., & Henson, P. W. (1986). A general method for optimizing tissue discrimination in magnetic resonance imaging. *Med. Phys.*, 13, 635-43.
- [23] Buxton, R. B., Edelman, R. R., Rosen, B. R., Wismer, G. L., & Brady, T. J. (1987). Contrast in rapid MR imaging: T1- and T2-weighted imaging. *J. Comput. Assist. Tomogr.*, 11, 7-16.
- [24] Wehrli, F. W., MacFall, J. R., Glover, G. H., Grigsby, N., Haughton, V., & Johanson, J. (1984). The dependence of nuclear magnetic resonance (NMR) image contrast on intrinsic and pulse sequence timing parameters. *J. Magn. Reson. Imag.*, 2, 3-16.
- [25] Moonen, C. T. W., van Zijl, P. C. M., Frank, J. A., LeBihan, D., & Becker, E. D. (1990). Functional magnetic resonance imaging in medicine and physiology. *Science*, 250, 53-61.
- [26] Wedeen, V. J., Meuli, R. A., Edelman, R. R., Geller, S. C., Frank, L. A., Brady, T. J., & Rosen, B. R. (1988). Projective imaging of pulsatile flow with magnetic resonance. *Science*, 230, 946-8.
- [27] Edelman, R. R., Mattle, H. P., Atkinson, D. J., & Hoogewood, H. M. (1990). MR angiography. *AJR*, 154, 937-46.
- [28] Listerud, J. (1991). First principles of magnetic resonance angiography. *Magn. Reson. Quart.*, 7, 136-70.
- [29] Carr, H. Y., & Purcell, E. M. (1954). Effects of diffusion on free precession in nuclear magnetic resonance experiments. *Phys. Rev.*, 94, 630-5.
- [30] Stejskal, E. O., & Tanner, J. E. (1965). Spin-diffusion measurements: Spin echoes in the presence of a time-dependent field gradient. *J. Chem. Phys.*, 42, 288-92.
- [31] LeBihan, D., Turner, R., Moonen, C. T., & Pekar, J. (1991). Imaging of diffusion and microcirculation with gradient sensitization: Design, strategy, and significance. *JMRI*, 1, 7-28.
- [32] LeBihan, D., Breton, E., Lallemand, D., Aubin, M.-L., Vignaud, J., & Laval-Jeantet, M. (1988). Separation of diffusion and perfusion in intravoxel incoherent motion MR imaging. *Radiology*, 168, 497-505.
- [33] SMRM Workshop (1991). Future directions in MRI of diffusion and perfusion. *Magn. Reson. Med.*, 19, 209-333.
- [34] LeBihan, D. (1990). Magnetic resonance imaging of perfusion. *Magn. Reson. Med.*, 14, 283-92.
- [35] Detre, J. A., Leigh, J. S., Williams, D. S., & Koretsky, A. P. (1992). Perfusion imaging. *Magn. Reson. Med.*, 23, 37-45.
- [36] LeBihan, D. (1992). Theoretical principles of perfusion imaging: Applications to magnetic resonance imaging. *Invest. Radiol.*, 27, S6-S11.
- [37] Detre, J. A., Zhang, W., Roberts, D. A., Silva, A. C., Williams, D. S., Grandis, D. J., Koretsky, A. P., & Leigh, J. S. (1994). Tissue-specific perfusion imaging using arterial spin labeling. *NMR in Biomedicine*, 7, 75-82.

- [38] Edelman, R. R., Sievert, B., Wielopolski, P., Pearlman, J., & Warach, S. (1994). Noninvasive mapping of cerebral perfusion by using EPISTAR MR angiography [Abstract]. *JMRI*, 4(P), 68.
- [39] Edelman, R., Wielopolski, P., & Schmitt, F. (1994). Echo-planar MR imaging. *Radiology*, 192, 600-12.
- [40] Edelman, R. R., Siewert, B., Adamis, M., Gaa, J., Laub, G., & Wielopolski, P. (1994). Signal targeting with alternating radiofrequency (STAR) sequences: Application to MR angiography. *Magn. Reson. Med.*, 31, 233-8.
- [41] Wolff, S. D., & Balaban, R. S. (1989). Magnetization transfer contrast (MTC) and tissue water proton relaxation in vivo. *Magn. Reson. Med.*, 10, 135-44.
- [42] Balaban, R. S., & Ceckler, T. L. (1992). Magnetization transfer contrast in magnetic resonance imaging. *Magn. Reson. Quart.*, 8, 116-37.
- [43] Brown, T. R., Kincaid, B. M., & Ugurbil, K. (1982). NMR chemical shift imaging in three dimensions. *Proc. Nat. Acad. Sci. USA*, 79, 3523-6.
- [44] Maudsley, A. A., Hilal, S. K., Perman, W. H., & Simon, H. E. (1983). Spatially resolved high resolution spectroscopy by "four dimensional" NMR. *J. Magn. Reson. Med.*, 52, 147-51.
- [45] Schenck, J. F. (1992). Health and physiological effects of human exposure to whole-body four-tesla magnetic fields during MRI. *Annals of the New York Academy of Sciences*, 649, 285-301.
- [46] Pauling, L., & Coryell, C. D. (1936). The magnetic properties and structure of hemoglobin, oxyhemoglobin, and carbonmonoxyhemoglobin. *Proc. Nat. Acad. Sci. USA*, 22, 210-16.
- [47] Thulborn, K. R., Waterton, J. C., Matthews, P. M., & Radda, G. K. (1982). Oxygenation dependence of the transverse relaxation time of water protons in whole blood at high field. *Biochim. Biophys. Acta*, 714, 265-70.
- [48] Brindle, K. M., Brown, F. F., Campbell, I. D., Grathwohl, C., & Kuchell, P. W. (1979). Application of spin-echo nuclear magnetic resonance to whole-cell systems. *Biochem. J.*, 180, 37-44.
- [49] Weisskoff, R. M., & Kiühne, S. (1992). MRI susceptometry: Image-based measurement of absolute susceptibility of MR contrast agents and human blood. *Magn. Reson. Med.*, 24, 375-83.
- [50] Brooks, R. A., & Chiro, G. D. (1987). Magnetic resonance imaging of stationary blood: A review. *Med. Phys.*, 14, 903-13.
- [51] Gomori, J. M., Grossman, R. J., Yu-IP, C., & Asakura, T. (1987). NMR relaxation times of blood: Dependence on field strength, oxidation state, and cell integrity. *J. Comput. Assist. Tomogr.*, 11, 684-90.
- [52] Matwiyoff, N. A., Gasparovic, C., Mazurchuk, R., & Matwiyoff, G. (1990). The line shapes of the water proton resonances of red blood cells containing carbonyl hemoglobin, deoxyhemoglobin, and methemoglobin: Implications for the interpretation of proton MRI at 1.5 T and below. *Magn. Reson. Imag.*, 8, 295-301.
- [53] Hayman, L. A., Ford, J. J., Taber, K. H., Saleem, A., Round, M. E., & Bryan, R. N. (1988). T2 effects of hemoglobin concentration: Assessment with in vitro MR spectroscopy. *Radiology*, 168, 489-91.
- [54] Janick, P. A., Hackney, D. B., Grossman, R. I., & Asakura, T. (1991). MR imaging of various oxidation states of intracellular and extracellular hemoglobin. *AJNR*, 12, 891-7.
- [55] Wright, G. A., Nishimura, D. G., & Macovski, A. (1991). Flow-independent magnetic resonance projection angiography. *Magn. Reson. Med.*, 17, 126-40.
- [56] Wright, G. A., Hu, B. S., & Macovski, A. (1991). Estimating oxygen saturation of blood in vivo with MR imaging at 1.5 T. *JMRI*, 1, 275-83.
- [57] Thulborn, K. R., & Brady, T. J. (1989). Iron in magnetic resonance imaging of cerebral hemorrhage. *Magn. Reson. Quart.*, 5, 23-38.
- [58] Hoppel, B. E., Weisskoff, R. M., Thulborn, K. R., Moore, J. B., Kwong, K. K., & Rosen, B. R. (1993). Measurement of regional blood oxygenation and cerebral hemodynamics. *Magn. Reson. Med.*, 30, 715-23.
- [59] Lauffer, R. B. (1990). Magnetic resonance contrast media: Principles and progress. *Magn. Reson. Quart.*, 6, 65-84.
- [60] SMRM Workshop (1991). Contrast enhanced magnetic resonance. *Magn. Reson. Med.*, 22, 177-378.
- [61] Bloembergen, N., Purcell, E. M., & Pound, R. V. (1948). Relaxation effects in nuclear magnetic resonance absorption. *Phys. Rev.*, 73, 679.
- [62] Rosen, B. R., Belliveau, J. W., & Chien, D. (1989). Perfusion imaging by nuclear magnetic resonance. *Magn. Reson. Quart.*, 5, 263-81.
- [63] Villringer, A., Rosen, B. R., Belliveau, J. W., Ackerman, J. L., Lauffer, R. B., Buxton, R. B., Chao, Y.-S., Wedeen, V. J., & Brady, T. J. (1988). Dynamic imaging with lanthanide chelates in normal brain: Contrast due to magnetic susceptibility effects. *Magn. Reson. Med.*, 6, 164-74.
- [64] Rosen, B. R., Belliveau, J. W., Vevea, J. M., & Brady, T. J. (1990). Perfusion imaging with NMR contrast agents. *Magn. Reson. Med.*, 14, 249-65.
- [65] Donahue, K. M., Burstein, D., Manning, W. J., & Gray, M. L. (1994). Studies of Gd-DTPA relaxivity and proton exchange rates in tissue. *Magn. Reson. Med.*, 32, 66-76.
- [66] Kennan, R. P., Zhong, J., & Gore, J. C. (1994). Intravascular susceptibility contrast mechanisms in tissues. *Magn. Reson. Med.*, 31, 9-21.
- [67] Fisel, C. R., Ackerman, J. L., Buxton, R. B., Garrido, L., Belliveau, J. W., Rosen, B. R., & Brady, T. J. (1991). MR contrast due to microscopically heterogeneous magnetic susceptibility: Numerical simulations and applications to cerebral physiology. *Magn. Reson. Med.*, 17, 336-47.
- [68] Yablonsky, D. A., & Haacke, E. M. (1994). Theory of NMR signal behavior in magnetically inhomogeneous tissues: The static dephasing regime. *Magn. Reson. Med.*, 32, 749-63.
- [69] Gillis, P., & Koenig, S. H. (1987). Transverse relaxation of solvent protons induced by magnetized spheres: Applications to ferritin, erythrocytes, and magnetite. *Magn. Reson. Med.*, 5, 323-45.
- [70] Hardy, P. A., & Henkleman, R. M. (1991). On the transverse relaxation rate enhancement induced by diffusion of spins through inhomogeneous fields. *Magn. Reson. Med.*, 17, 348-56.
- [71] Hardy, P. A., & Henkleman, R. M. (1989). Transverse relaxation rate enhancement caused by magnetic particulates. *Magn. Reson. Imag.*, 7, 265-75.
- [72] Chu, S. C.-K., Xu, Y., Balschi, J. A., & Springer, C. S., Jr. (1990). Bulk magnetic susceptibility shifts in NMR studies

- of compartmentalized samples: Use of paramagnetic reagents. *Magn. Reson. Med.*, 13, 239–62.
- [73] Weisskoff, R. M., Hoppel, B. J., & Rosen, B. R. (1992). Signal changes in dynamic contrast studies: Theory and experiment in vivo [Abstract]. *JMRI*, 2(P), 77.
- [74] Boxerman, J. L., Weisskoff, R. M., Hoppel, B. E., & Rosen, B. R. (1993). MR contrast due to microscopically heterogeneous magnetic susceptibility: Cylindrical geometry. In *Proceedings of the 12th Annual Meeting of the SMRM* (New York), p. 389.
- [75] Edmister, W. B., & Weisskoff, R. M. (1993). Diffusion effects on T2 relaxation in microscopically inhomogeneous magnetic fields. In *Proceedings of the 12th Annual Meeting of the SMRM* (New York), p. 799.
- [76] Weisskoff, R. M., Zuo, C. S., Boxerman, J. L., & Rosen, B. R. (1994). Microscopic susceptibility variation and transverse relaxation: Theory and experiment. *Magn. Reson. Med.*, 31, 601–10.
- [77] Ogawa, S., Menon, R. S., Tank, D. W., Kim, S.-G., Merkle, H., Ellerman, J. M., & Ugurbil, K. (1993). Functional brain mapping by blood oxygenation level-dependent contrast magnetic resonance imaging: A comparison of signal characteristics with a biophysical model. *Biophysical J.*, 64, 803–12.
- [78] Wong, E. C., & Bandettini, P. A. (1993). A deterministic method for computer modelling of diffusion effects in MRI with application to BOLD contrast imaging. In *Proceedings of the 12th Annual Meeting of the SMRM* (New York), p. 10.
- [79] Li, C. S., Frisk, T. A., & Smith, M. B. (1993). Computer simulations of susceptibility effects: Implications for line-shapes and frequency shifts in localized spectroscopy of the human head. In *Proceedings of the 12th Annual Meeting of the SMRM* (New York), p. 912.
- [80] Williams, D. S., Detre, J. A., Leigh, J. S., & Koretsky, A. S. (1992). Magnetic resonance imaging of perfusion using spin-inversion of arterial water. *Proc. Nat. Acad. Sci. USA*, 89, 212–16.
- [81] Kwong, K. K., Chesler, D. A., Weisskoff, R. M., & Rosen, B. R. (1994). Perfusion MR imaging. In *Proceedings of the 2nd Annual Meeting of the SMR* (San Francisco), p. 1005.
- [82] Wong, E. C., Buxton, R. B., & Frank, L. R. (1997). Implementation of quantitative perfusion imaging techniques for functional brain mapping using pulsed arterial spin labeling. *NMR in Biomedicine*, 10, 237–49.
- [83] Wong, E. C., Buxton, R. B., & Frank, L. R. (1998). Quantitative imaging of perfusion using a single subtraction (QUIPSS and QUIPSSII). *Magn. Reson. Med.*, 39, 702–8.
- [84] Kim, S.-G. (1995). Quantification of relative cerebral blood flow change by flow-sensitive alternating inversion recovery (FAIR) technique: Application to functional mapping. *Magn. Reson. Med.*, 34, 293–301.
- [85] Ogawa, S., Lee, T. M., Kay, A. R., & Tank, D. W. (1990). Brain magnetic resonance imaging with contrast dependent on blood oxygenation. *Proc. Nat. Acad. Sci. USA*, 87, 9868–72.
- [86] Turner, R., LeBihan, D., Moonen, C. T. W., Despres, D., & Frank, J. (1991). Echo-planar time course MRI of cat brain oxygenation changes. *Magn. Reson. Med.*, 22, 159–66.
- [87] Ogawa, S., & Lee, T. M. (1992). Functional brain imaging with physiologically sensitive image signals [Abstract]. *JMRI*, 2(P) (WIP Suppl.), S22.
- [88] Haacke, E. M., Lai, S., Reichenbach, J. R., Kuppusamy, K., Hoogenraad, F. G. C., Takeichi, H., & Lin, W. (1997). In vivo measurement of blood oxygen saturation using magnetic resonance imaging: A direct validation of the blood oxygen level-dependent concept in functional brain imaging. *Human Brain Mapping*, 5, 341–6.
- [89] Davis, T. L., Kwong, K. K., Weisskoff, R. M., & Rosen, B. R. (1998). Calibrated functional MRI: Mapping the dynamics of oxidative metabolism. *Proc. Nat. Acad. Sci. USA*, 95, 1834–9.
- [90] Kim, S.-G., & Ugurbil, K. (1997). Comparison of blood oxygenation and cerebral blood flow effects in fMRI: Estimation of relative oxygen consumption change. *Magn. Reson. Med.*, 38, 59–65.
- [91] van Zijl, P. C. M., Eleff, S. M., Ulatowski, J. A., Oja, J. M. E., Ulug, A. M., Traystman, R. J., & Kauppinen, R. A. (1998). Quantitative assessment of blood flow, blood volume, and blood oxygenation effects in functional magnetic resonance imaging. *Nature Medicine*, 4, 159–67.
- [92] Belliveau, J. W., Rosen, B. R., Kantor, H. L., Rzedzian, R. R., Kennedy, D. N., McKinstry, R. C., Vevea, J. M., Cohen, M. S., Pykett, I. L., & Brady, T. J. (1990). Functional cerebral imaging by susceptibility-contrast NMR. *Magn. Reson. Med.*, 14, 538–46.
- [93] Mansfield, P. (1977). Multi-planar image formation using NMR spin echoes. *J. Phys.*, C10, L55–L58.
- [94] Stehling, M. K., Turner, R., & Mansfield, P. (1991). Echo-planar imaging: Magnetic resonance imaging in a fraction of a second. *Science*, 254, 43–50.
- [95] Cohen, M. S., & Weisskoff, R. M. (1991). Ultra-fast imaging. *Magn. Reson. Imag.*, 9, 1–37.
- [96] Kwong, K. K. (1995). Functional magnetic resonance imaging with echo planar imaging. *Magn. Reson. Quart.*, 11, 1–20.
- [97] Kwong, K. K., Chesler, D. A., Weisskoff, R. M., Donahue, K. M., Davis, T. L., Ostergaard, L., Campbell, T. A., & Rosen, B. R. (1995). MR perfusion studies with T1-weighted echo planar imaging. *Magn. Reson. Med.*, 34, 878–87.
- [98] Wong, E. C., Buxton, R. B., & Frank, L. R. (1996). Quantitative imaging of perfusion using a single subtraction (QUIPSS). In *Proceedings of the 2nd International Conference on Functional Mapping of the Human Brain* (Boston), p. 5.
- [99] Chesler, D. A., & Kwong, K. K. (1995). An intuitive guide to the T1 based perfusion model. *Int. J. Imag. Syst. & Tech.*, 6, 171–4.
- [100] Buxton, R. B., Wong, E. C., & Frank, L. R. (1995). A quantitative model for EPSTAR perfusion imaging. In *Proceedings of the 3rd Annual Meeting of the SMR* (Nice), p. 132.
- [101] Ogawa, S., Lee, T.-M., Nayak, A. S., & Glynn, P. (1990). Oxygenation-sensitive contrast in magnetic resonance image of rodent brain at high magnetic fields. *Magn. Reson. Med.*, 14, 68–78.
- [102] Ogawa, S., & Lee, T.-M. (1990). Magnetic resonance imaging of blood vessels at high fields: In vivo and in vitro

- measurements and image simulation. *Magn. Reson. Med.*, 16, 9–18.
- [103] Brady, T. J. (1991). Future prospects for MR imaging. In *Proceedings of the 10th Annual Meeting of the SMRM* (San Francisco), p. 2.
- [104] Grinvald, A., Frostig, R. D., Siegel, R. M., & Bratsfeld, E. (1991). High-resolution optical imaging of functional brain architecture in the awake monkey. *Proc. Nat. Acad. Sci. USA*, 88, 11559–63.
- [105] Frostig, R. D., Lieke, E. E., Ts'o, D. Y., & Grinvald, A. (1990). Cortical functional architecture and local coupling between neuronal activity and the microcirculation revealed by in vivo high-resolution optical imaging of intrinsic signals. *Proc. Nat. Acad. Sci. USA*, 87, 6082–6.
- [106] Fox, P. T., & Raichle, M. E. (1986). Focal physiological uncoupling of cerebral blood flow and oxidative metabolism during somatosensory stimulation in human subjects. *Proc. Nat. Acad. Sci. USA*, 83, 1140–4.
- [107] Bandettini, P. A., & Wong, E. C. (1997). Magnetic resonance imaging of human brain function: Principles, practicalities, and possibilities. *Neurosurgery Clinics of North America*, 8, 345–71.
- [108] Frahm, J., Merboldt, K.-D., & Hanicke, W. (1993). Functional MRI of human brain activation at high spatial resolution. *Magn. Reson. Med.*, 29, 139–44.
- [109] Kim, S.-G., Ashe, J., Georgopoulos, A. P., Merkle, H., Ellermann, J. M., Menon, R. S., Ogawa, S., & Ugurbil, K. (1993). Functional imaging of human motor cortex at high magnetic field. *J. Neurophysiol.*, 69, 297–302.
- [110] Noll, D. C. (1995). Methodologic considerations for spiral *k*-space functional MRI. *Int. J. Imag. Syst. & Tech.*, 6, 175–83.
- [111] Glover, G. H., & Lee, A. T. (1995). Motion artifacts in fMRI: Comparison of 2DFT with PR and spiral scan methods. *Magn. Reson. Med.*, 33, 624–35.
- [112] Schmitt, F., Stehling, M., & Turner, R. (1998). *Echo-Planar Imaging: Theory, Technique, and Application*. Berlin: Springer-Verlag.
- [113] Butts, K., Riederer, S. J., Ehman, R. L., Thompson, R. M., & Jack, C. R. (1994). Interleaved echo planar imaging on a standard MRI system. *Magn. Reson. Med.*, 31, 67–72.
- [114] McKinnon, G. C. (1993). Ultrafast interleaved gradient-echo-planar imaging on a standard scanner. *Magn. Reson. Med.*, 30, 609–16.
- [115] Le, T. H., & Hu, X. (1996). Retrospective estimation and correction of physiological artifacts in fMRI by direct extraction of physiological activity from MR data. *Magn. Reson. Med.*, 35, 290–8.
- [116] Hu, X., & Kim, S.-G. (1994). Reduction of signal fluctuations in functional MRI using navigator echoes. *Magn. Reson. Med.*, 31, 495–503.
- [117] Biswal, B., Jesmanowicz, A., & Hyde, J. S. (1997). High temporal resolution fMRI. In *Proceedings of the 5th Annual Meeting of the ISMRM* (Vancouver), p. 1629.
- [118] Buxton, R. B., Luh, W. M., Wong, E. C., Frank, L. R., & Bandettini, P. A. (1998). Diffusion-weighting attenuates the BOLD signal change but not the post-stimulus undershoot. In *Proceedings of the 6th Annual Meeting of the ISMRM* (Sydney), p. 7.
- [119] Frahm, J., Krüger, G., Merboldt, K.-D., & Kleinschmidt, A. (1996). Dynamic uncoupling and recoupling of perfusion and oxidative metabolism during focal activation in man. *Magn. Reson. Med.*, 35, 143–8.
- [120] Fransson, P., Krüger, G., Merboldt, K.-D., & Frahm, J. (1998). Temporal characteristics of oxygenation-sensitive responses to visual activation in humans. *Magn. Reson. Med.*, 39, 912–19.
- [121] DeYoe, E. A., Bandettini, P., Neitz, J., Miller, D., & Winans, P. (1994). Functional magnetic resonance imaging (fMRI) of the human brain. *J. Neuroscience Methods*, 54, 171–87.
- [122] Bandettini, P. A., Wong, E. C., Binder, J. R., Rao, S. M., Jesmanowicz, A., Aaron, E. A., Lowry, T. F., Forster, H. V., Hinks, R. S., & Hyde, J. S. (1995). Functional MRI using the BOLD approach: Dynamic characteristics and data analysis methods. In D. LeBihan (Ed.), *Diffusion and Perfusion: Magnetic Resonance Imaging*, pp. 335–49. New York: Raven.
- [123] Hennig, J., Janz, C., Speck, O., & Ernst, T. (1995). Functional spectroscopy of brain activation following a single light pulse: Examinations of the mechanism of the fast initial response. *Int. J. Imag. Syst. & Tech.*, 6, 203–8.
- [124] Menon, R. S., Ogawa, S., Strupp, J. P., Anderson, P., & Ugurbil, K. (1995). BOLD based functional MRI at 4 Tesla includes a capillary bed contribution: Echo-planar imaging correlates with previous optical imaging using intrinsic signals. *Magn. Reson. Med.*, 33, 453–9.
- [125] Hu, X., Le, T. H., & Ugurbil, K. (1997). Evaluation of the early response in fMRI in individual subjects using short stimulus duration. *Magn. Reson. Med.*, 37, 877–84.
- [126] Davis, T. L., Weisskoff, R. M., Kwong, K. K., Savoy, R., & Rosen, B. R. (1994). Susceptibility contrast undershoot is not matched by inflow contrast undershoot. In *Proceedings of the 2nd Annual Meeting of the SMR* (San Francisco), p. 435.
- [127] Bandettini, P. A., Kwong, K. K., Davis, T. L., Tootell, R. B. H., Wong, E. C., Fox, P. T., Belliveau, J. W., & Weisskoff, R. M. (1997). Characterization of cerebral blood oxygenation and flow changes during prolonged brain activation. *Human Brain Mapping*, 5, 93–109.
- [128] Friston, K. J., Jezzard, P., & Turner, R. (1994). Analysis of functional MRI time-series. *Human Brain Mapping*, 2, 69–78.
- [129] Bandettini, P. A., & Cox, R. W. (1998). Contrast in single-trial fMRI: Interstimulus interval dependency and comparison with blocked strategies. In *Proceedings of the 6th Annual Meeting of the ISMRM* (Sydney), p. 161.
- [130] Bandettini, P. A., & Cox, R. W. (submitted). Functional contrast in event-related fMRI: Theory and experiment. *Human Brain Mapping*.
- [131] Cohen, M. S. (1997). Parametric analysis of fMRI data using linear systems methods. *NeuroImage*, 6, 93–103.
- [132] Blamire, A. M., Ogawa, S., Ugurbil, K., Rothman, D., McCarthy, G., Ellermann, J. M., Hyder, F., Rattner, Z., & Shulman, R. G. (1992). Dynamic mapping of the human visual cortex by high-speed magnetic resonance imaging. *Proc. Nat. Acad. Sci. USA*, 89, 11069–73.
- [133] Bandettini, P. A., Wong, E. C., DeYoe, E. A., Binder, J. R., Rao, S. M., Birzer, D., Estkowski, L. D., Jesmanowicz,

- A., Hinks, R. S., & Hyde, J. S. (1993). The functional dynamics of blood oxygen level dependent contrast in the motor cortex. In *Proceedings of the 12th Annual Meeting of the SMRM* (New York), p. 1382.
- [134] Savoy, R. L., O'Craven, K. M., Weisskoff, R. M., Davis, T. L., Baker, J., & Rosen, B. (1994). Exploring the temporal boundaries of fMRI: Measuring responses to very brief visual stimuli. In *Book of Abstracts of the 24th Annual Meeting of the Society for Neuroscience* (Miami), p. 1264.
- [135] Savoy, R. L., Bandettini, P. A., Weisskoff, R. M., Kwong, K. K., Davis, T. L., Baker, J. R., Weisskoff, R. M., & Rosen, B. R. (1995). Pushing the temporal resolution of fMRI: Studies of very brief visual stimuli, onset variability and asynchrony, and stimulus-correlated changes in noise. In *Proceedings of the 3rd Annual Meeting of the SMR* (Nice), p. 450.
- [136] Buckner, R. L., Bandettini, P. A., O'Craven, K. M., Savoy, R. L., Peterson, S. E., Raichle, M. E., & Rosen, B. R. (1996). Detection of cortical activation during averaged single trials of a cognitive task using functional magnetic resonance imaging. *Proc. Nat. Acad. Sci. USA*, 93, 14878-83.
- [137] Birn, R. M., Bandettini, P. A., Cox, R. W., & Shaker, R. (1999). Event-related fMRI of tasks involving brief motion. *Human Brain Mapping*, 7, 106-14.
- [138] Buckner, R. L., Goodman, J., Burock, M., Rotte, M., Koutstaal, W., Schacter, D., Rosen, B., & Dale, A. M. (1998). Functional-anatomic correlates of object priming in humans revealed by rapid presentation event-related fMRI. *Neuron*, 20, 285-96.
- [139] Burock, M. A., Buckner, R. L., & Dale, A. M. (1998). Understanding differential responses in event related fMRI through linear simulation. In *Proceedings of the 6th Annual Meeting of the ISMRM* (Sydney), p. 245.
- [140] Friston, K. J., Josephs, O., Rees, G., & Turner, R. (1998). Nonlinear event-related responses in fMRI. *Magn. Reson. Med.*, 39, 41-52.
- [141] Friston, K. J., Fletcher, P., Josephs, O., Holmes, A., Rugg, M. D., & Turner, R. (1998). Event-related fMRI: Characterizing differential responses. *NeuroImage*, 7, 30-40.
- [142] Josephs, O., Turner, R., & Friston, K. (1997). Event-related fMRI. *Human Brain Mapping*, 5, 243-8.
- [143] McCarthy, G., Luby, M., Gore, J., & Goldman-Rakic, P. (1997). Infrequent events transiently activate human prefrontal and parietal cortex as measured by functional MRI. *J. Neurophysiology*, 77, 1630-4.
- [144] Rosen, B. R., Buckner, R. L., & Dale, A. M. (1998). Event-related functional MRI: Past, present, future. *Proc. Nat. Acad. Sci. USA*, 95, 773-80.
- [145] Schacter, D. L., Buckner, R. L., Koutstaal, W., Dale, A. M., & Rosen, B. R. (1997). Late onset of anterior prefrontal activity during true and false recognition: An event related fMRI study. *NeuroImage*, 6, 259-69.
- [146] Hickok, G., Love, T., Swinney, D., Wong, E. C., & Buxton, R. B. (1997). Functional MR imaging during auditory word perception: A single-trial presentation paradigm. *Brain and Language*, 58, 197-201.
- [147] Luknowsky, D. C., Gati, J. S., & Menon, R. S. (1998). Mental chronometry using single trials and EPI at 4T. In *Proceedings of the 6th Annual Meeting of the ISMRM* (Sydney), p. 167.
- [148] Konishi, S., Yoneyama, R., Itagaki, H., Uchida, I., Nakajima, K., Kato, H., Okajima, K., Koizumi, H., & Miyashita, Y. (1996). Transient brain activity used in magnetic resonance imaging to detect functional areas. *NeuroReport*, 8, 19-23.
- [149] Clark, V. P., Maisog, J. M., & Haxby, J. V. (in press). An fMRI study of face perception and memory using random stimulus sequences. *J. Neurophys.*
- [150] Boynton, G. M., Engel, S. A., Glover, G. H., & Heeger, D. J. (1996). Linear systems analysis of functional magnetic resonance imaging in human V1. *J. Neuroscience*, 16, 4207-21.
- [151] Dale, A. M., & Buckner, R. L. (1997). Selective averaging of rapidly presented individual trials using fMRI. *Human Brain Mapping*, 5, 329-40.
- [152] Zarahn, E., Aguirre, G., & D'Esposito, M. (1997). A trial-based experimental design for fMRI. *NeuroImage*, 6, 122-38.
- [153] Buckner, R. L., & Koutstaal, W. (1998). Functional neuroimaging studies of encoding, priming, and explicit memory retrieval. *Proc. Nat. Acad. Sci. USA*, 95, 891-8.
- [154] Buckner, R. L., Koutstaal, W., Schacter, D. L., Wagner, A. D., & Rosen, B. R. (1998). Functional-anatomic study of episodic retrieval using fMRI. *NeuroImage*, 7, 151-62.
- [155] Friston, K. J., Frith, C. D., Turner, R., & Frackowiak, R. S. J. (1995). Characterizing evoked hemodynamics with fMRI. *NeuroImage*, 2, 157-65.
- [156] Vasquez, A., & Noll, D. (1998). Nonlinear aspects of the BOLD response in functional MRI. *NeuroImage*, 7, 108-18.
- [157] Birn, R. M., Bandettini, P. A., Cox, R. W., & Shaker, R. (1998). fMRI during stimulus correlated motion and overt subject responses using a single trial paradigm. In *Proceedings of the 6th Annual Meeting of the ISMRM* (Sydney), p. 159.
- [158] Buxton, R. B., Wong, E. C., & Frank, L. R. (1998). Dynamics of blood flow and oxygenation changes during brain activation: The balloon model. *Magn. Reson. Med.*, 39, 855-64.
- [159] Menon, R. S., Ogawa, S., & Ugurbil, K. (1995). High-temporal-resolution studies of the human primary visual cortex at 4T: Teasing out the oxygenation contribution in fMRI. *Int. J. Imag. Syst. & Tech.*, 6, 209-15.
- [160] Richter, W., Andersen, P. M., Georgopoulos, A. P., & Kim, S.-G. (1997). Sequential activity in human motor areas during a delayed cued finger movement task studied by time-resolved fMRI. *NeuroReport*, 8, 1257-61.
- [161] Kim, S.-G., Richter, W., & Ugurbil, K. (1997). Limitations of temporal resolution in functional MRI. *Magn. Reson. Med.*, 37, 631-6.
- [162] Richter, W., Ugurbil, K., Georgopoulos, A., & Kim, S.-G. (1997). Time-resolved fMRI of mental rotation. *NeuroReport*, 8, 3697-3702.
- [163] Courtney, S. M., Ungerleider, L. G., Keil, K., & Haxby, J. V. (1997). Transient and sustained activity in a distributed neural system for human working memory. *Nature*, 386, 608-11.
- [164] Binder, J. R., Jesmanowicz, A., Rao, S. M., Bandettini, P. A., Hammeke, T. A., & Hyde, J. S. (1993). Analysis of phase differences in periodic functional MRI activation

- data. In *Proceedings of the 12th Annual Meeting of the SMRM* (New York), p. 1383.
- [165] Lee, A. T., Glover, G. H., & Meyer, C. H. (1995). Discrimination of large venous vessels in time-course spiral blood-oxygen-level-dependent magnetic-resonance functional neuroimaging. *Magn. Reson. Med.*, 33, 745–54.
- [166] Bandettini, P. A. (1995). Magnetic resonance imaging of human brain activation using endogenous susceptibility contrast. Doctoral dissertation, Medical College of Wisconsin.
- [167] Saad, Z. S., Ropella, K. M., Carman, G. J., & DeYoe, E. A. (1996). Temporal phase variation of fMRI signals in vasculature versus parenchyma. In *Proceedings of the 4th Annual Meeting of the ISMRM* (New York), p. 1834.
- [168] Luknowsky, D. C., Gati, J. S., & Menon, R. S. (1998). Mental chronometry using single trials and EPI at 4T. In *Proceedings of the 6th Annual Meeting of the ISMRM* (Sydney), p. 167.
- [169] Frostig, R. D. (1994). What does in vivo optical imaging tell us about the primary visual cortex in primates? In A. Peters & K. S. Rockland (Eds.), *Cerebral Cortex*, vol. 10, p. 331. New York: Plenum.
- [170] Turner, R., Jezzard, P., Bihan, D. L., & Prinster, A. (1993). Contrast mechanisms and vessel size effects in BOLD contrast functional neuroimaging. In *Proceedings of the 12th Annual Meeting of the SMRM* (New York), p. 173.
- [171] Frahm, J., Merboldt, K.-D., Hancike, W., Kleinschmidt, A., & Boecker, H. (1994). Brain or vein-oxygenation or flow? On signal physiology in functional MRI of human brain activation. *NMR in Biomedicine*, 7, 45–53.
- [172] Haacke, E. M., Hopkins, A., Lai, S., Buckley, P., Friedman, L., Meltzer, H., Hedera, P., Friedland, R., Thompson, L., Detterman, D., Tkach, J., & Lewin, J. S. (1994). 2D and 3D high resolution gradient-echo functional imaging of the brain: Venous contributions to signal in motor cortex studies. *NMR in Biomedicine*, 7, 54–62.
- [173] Lai, S., Hopkins, A. L., Haacke, E. M., Li, D., Wasserman, B. A., Buckley, P., Friedman, L., Meltzer, H., Hedera, P., & Friedland, R. (1993). Identification of vascular structures as a major source of signal contrast in high resolution 2D and 3D functional activation imaging of the motor cortex at 1.5T: Preliminary results. *Magn. Reson. Med.*, 30, 387–92.
- [174] Wong, E. C., Bandettini, P. A., & Hyde, J. S. (1992). Echo-planar imaging of the human brain using a three axis local gradient coil. In *Proceedings of the 11th Annual Meeting of the SMRM* (Berlin), p. 105.
- [175] Ugurbil, K., Garwood, M., Ellermann, J., Hendrich, K., Hinke, R., Hu, X., Kim, S.-G., Menon, R., Merkle, H., Ogawa, S., & Salmi, R. (1993). Imaging at high magnetic fields: Initial experiences at 4 T. *Magn. Reson. Quart.*, 9, 259–77.
- [176] Engel, S. A., Rumelhart, D. E., Wandell, B. A., Lee, A. T., Glover, G. H., Chichilnisky, E. J., & Shadlen, M. N. (1994). fMRI of human visual cortex. *Nature*, 369, 525. [Erratum, vol. 370, p. 106.]
- [177] Schneider, W., Noll, D. C., & Cohen, J. D. (1993). Functional topographic mapping of the cortical ribbon in human vision with conventional MRI scanners. *Nature*, 365, 150–3.
- [178] Sereno, M. I., Dale, A. M., Reppas, J. R., Kwong, K. K., Belliveau, J. W., Brady, T. J., Rosen, B. R., & Tootell, R. B. H. (1995). Functional MRI reveals borders of multiple visual areas in humans. *Science*, 268, 889–93.
- [179] DeYoe, E. A., Carman, G., Bandettini, P., Glickman, S., Weiser, J., Cox, R., Miller, D., & Neitz, J. (1996). Mapping striate and extrastriate areas in human cerebral cortex. *Proc. Nat. Acad. Sci. USA*, 93, 2382–6.
- [180] Fox, P. T., & Raichle, M. E. (1985). Stimulus rate determines regional brain blood flow in striate cortex. *Ann. Neurol.*, 17, 303–5.
- [181] Tootell, R. B. H., Reppas, J. B., Kwong, K. K., Malach, R., Born, R. T., Brady, T. J., Rosen, B. R., & Belliveau, J. W. (1995). Functional analysis of human MT and related visual cortical areas using magnetic resonance imaging. *J. Neuroscience*, 15, 3215–30.
- [182] DeYoe, E. A., Schmit, P. W., & Neitz, J. (1995). Distinguishing cortical areas that are sensitive to task and stimulus variables with fMRI. In *Book of Abstracts of the 25th Annual Meeting of the Society for Neuroscience* (San Diego), p. 1750.
- [183] Rao, S. M., Bandettini, P. A., Binder, J. R., Bobholz, J., Hammeke, T. A., Stein, E. A., & Hyde, J. S. (1996). Relationship between finger movement rate and functional magnetic resonance signal change in human primary motor cortex. *J. Cereb. Blood Flow & Metab.*, 16, 1250–4.
- [184] Binder, J. R., Rao, S. M., Hammeke, T. A., Frost, J. A., Bandettini, P. A., & Hyde, J. S. (1994). Effects of stimulus rate on signal response during functional magnetic resonance imaging of auditory cortex. *Cognitive Brain Research*, 2, 31–8.
- [185] Guimaraes, A. R., Baker, J. R., & Weisskoff, R. M. (1995). Cardiac-gated functional MRI with T1 correction. In *Proceedings of the 3rd Annual Meeting of the SMR* (Nice), p. 798.
- [186] Bandettini, P. A., Jesmanowicz, A., Wong, E. C., & Hyde, J. S. (1993). Processing strategies for time-course data sets in functional MRI of the human brain. *Magn. Reson. Med.*, 30, 161–73.
- [187] Gold, S., Shristian, B., Arndt, S., Zeien, G., Cizadlo, T., Johnson, D. L., Flaum, M., & Andreasen, N. C. (1998). Functional MRI statistical software packages: A comparative analysis. *Human Brain Mapping*, 6, 73–84.
- [188] Jezzard, P., LeBihan, D., Cuenod, C., Pannier, L., Prinster, A., & Turner, R. (1993). An investigation of the contributions of physiological noise in human functional MRI studies at 1.5 Tesla and 4 Tesla. In *Proceedings of the 12th Annual Meeting of the SMRM* (New York), p. 1392.
- [189] Weisskoff, R. M., Baker, J., Belliveau, J., Davis, T. L., Kwong, K. K., Cohen, M. S., & Rosen, B. R. (1993). Power spectrum analysis of functionally-weighted MR data: What's in the noise? In *Proceedings of the 12th Annual Meeting of the SMRM* (New York), p. 7.
- [190] Cohen, J. D., Noll, D. C., & Schneider, W. (1993). Functional magnetic resonance imaging: Overview and methods for psychological research. *Behavior Research Methods, Instruments, and Computers*, 25, 101–13.
- [191] Binder, J. R., Rao, S. M., Hammeke, T. A., Bandettini, P. A., Jesmanowicz, A., Frost, J. A., Wong, E. C., Haughton, V. M., & Hyde, J. S. (1993). Temporal characteristics of

- functional magnetic resonance signal changes in lateral frontal and auditory cortex. In *Proceedings of the 12th Annual Meeting of the SMRM* (New York), p. 5.
- [192] DeYoe, E. A., Neitz, J., Bandettini, P. A., Wong, E. C., & Hyde, J. S. (1992). Time course of event-related MR signal enhancement in visual and motor cortex. In *Proceedings of the 11th Annual Meeting of the SMRM* (Berlin), p. 1824.
- [193] Lee, A. T., Meyer, C. H., & Glover, G. H. (1993). Discrimination of large veins in time-course functional neuroimaging with spiral k -space trajectories [Abstract]. *JMRI*, 3(P), 59-60.
- [194] Noll, D. C., Cohen, J. D., Meyer, C. H., & Schneider, W. (1995). Spiral k -space MR imaging of cortical activation. *JMRI*, 5, 49-56.
- [195] Wong, E. C., Boskamp, E., & Hyde, J. S. (1992). A volume optimized quadrature elliptical endcap birdcage brain coil. In *Proceedings of the 11th Annual Meeting of the SMRM* (Berlin), p. 4015.
- [196] Farzaneh, F., Riederer, S. J., & Pelc, N. J. (1990). Analysis of T2 limitations and off-resonance effects in spatial resolution and artifacts in echo-planar imaging. *Magn. Reson. Med.*, 14, 123-39.
- [197] Blamire, A. M., & Shulman, R. G. (1994). Implementation of echo-planar imaging on an unmodified spectrometer at 2.1 Tesla for functional imaging. *Magn. Reson. Imag.*, 12, 669-71.
- [198] Jezzard, P., & Balaban, R. S. (1995). Correction for geometric distortion in echo planar images from B_0 field distortions. *Magn. Reson. Med.*, 34, 65-73.
- [199] Weisskoff, R. M., & Davis, T. L. (1992). Correcting gross distortion on echo planar images. In *Proceedings of the 11th Annual Meeting of the SMRM* (Berlin), p. 4515.
- [200] Song, A. W., Wong, E. C., & Hyde, J. S. (1994). Echo-volume imaging. *Magn. Reson. Med.*, 32, 668-71.
- [201] Duyn, J. H., Moonen, C. T. W., vanYperen, G. H., de Boer, R. W., & Luyten, P. R. (1994). Inflow versus deoxyhemoglobin effects in BOLD functional MRI using gradient-echoes at 1.5 T. *NMR in Biomedicine*, 7, 83-8.
- [202] Connelly, A., Jackson, G. D., Frackowiak, R. S. J., Belliveau, J. W., Vargha-Khadem, F., & Gadian, D. S. (1993). Functional mapping of activated human primary cortex with a clinical MR imaging system. *Radiology*, 188, 125-30.
- [203] Cao, Y., Towle, V. L., Levin, D. N., & Balter, J. M. (1993). Functional mapping of human motor cortical activation with conventional MR imaging at 1.5 T. *JMRI*, 3, 869-75.
- [204] Constable, R. T., McCarthy, G., Allison, T., Allison, A. W., Anderson, A. W., & Gore, J. C. (1994). Functional brain imaging at 1.5 T using conventional gradient echo MR imaging techniques. *Magn. Reson. Imag.*, 11, 451-9.
- [205] Hu, X., & Kim, S.-G. (1993). A new T2*-weighting technique for magnetic resonance imaging. *Magn. Reson. Med.*, 30, 512-17.
- [206] Wong, E. C., & Tan, S. G. (1994). A comparison of signal to noise ratio and BOLD contrast between single voxel spectroscopy and echo-planar imaging. In *Proceedings of the 2nd Annual Meeting of the SMR* (San Francisco), p. 663.
- [207] Liu, G., Sobering, G., Olson, A. W., von Gelderen, P., & Moonen, C. T. (1993). Fast echo-shifted gradient-recalled MRI: Combining a short repetition time with variable T2* weighting. *Magn. Reson. Med.*, 30, 68-75.
- [208] Moonen, C. T., Liu, G., von Gelderen, P., & Sobering, G. (1992). A fast gradient-recalled MRI technique with increased sensitivity to dynamic susceptibility effects. *Magn. Reson. Med.*, 26, 184-9.
- [209] Shaw, D. W., Weinberger, E., Hayes, C. E., Yuan, C., Stark, J. E., White, K. S., Radvilas, M., Young, G., & Foo, T. (1993). Reduced K-space (keyhole) functional imaging without contrast on a conventional clinical scanner. In *Proceedings of the 12th Annual Meeting of the SMRM* (New York), p. 1430.
- [210] Constable, R. T., Kennan, R. P., Puce, A., McCarthy, G., & Gore, J. C. (1994). Functional NMR imaging using fast spin echo at 1.5 T. *Magn. Reson. Med.*, 31, 686-90.
- [211] Glover, G. H., Lee, A. T., & Meyers, C. H. (1993). Motion artifacts in fMRI: Comparison of 2DFT with PR and spiral scan methods. In *Proceedings of the 12th Annual Meeting of the SMRM* (New York), p. 197.
- [212] Cohen, J. D., Forman, S. D., Casey, B. J., & Noll, D. C. (1993). Spiral-scan imaging of dorsolateral prefrontal cortex during a working memory task. In *Proceedings of the 12th Annual Meeting of the SMRM* (New York), p. 1405.
- [213] Turner, R., & Jezzard, P. (1994). Magnetic resonance studies of brain functional activation using echo-planar imaging. In R. W. Thatcher, M. Hallett, T. Zeffiro, E. R. John, & M. Huerta (Eds.), *Functional Neuroimaging: Technical Foundations*, pp. 69-78. San Diego: Academic Press.
- [214] Schulman, R. G., Blamire, A. M., Rothman, D. L., & McCarthy, G. (1993). Nuclear magnetic resonance imaging and spectroscopy of human brain function. *Proc. Nat. Acad. Sci. USA*, 90, 3127-33.
- [215] Binder, J. R., & Rao, S. M. (1994). Human brain mapping with functional magnetic resonance imaging. In A. Kertesz (Ed.), *Localization and Neuroimaging in Neuropsychology*, p. 185. San Diego: Academic Press.
- [216] Prichard, J. W., & Rosen, B. R. (1994). Functional study of the brain by NMR. *Journal of Cerebral Blood Flow and Metabolism*, 14, 365-72.
- [217] Cohen, M. E., & Bookheimer, S. Y. (1994). Localization of brain function using magnetic resonance imaging. *TINS*, 17, 1994.
- [218] Orrison, W. W., Lewine, J. D., Sanders, J. A., & Hartshorne, M. F. (1995). *Functional Brain Imaging*. St. Louis, MO: Mosby.
- [219] Bandettini, P. A., Binder, J. R., DeYoe, E. A., & Hyde, J. S. (1996). Sensory activation-induced hemodynamic changes observed in the human brain with echo planar MRI. In D. M. Grant & R. K. Harris (Eds.), *Encyclopedia of Nuclear Magnetic Resonance*, pp. 1051-6. Chichester, U.K.: Wiley.
- [220] Bandettini, P. A., Binder, J. R., DeYoe, E. A., Rao, S. M., Jesmanowicz, A., Hammeke, T. A., Haughton, V. M., Wong, E. C., & Hyde, J. S. (1995). Functional MRI using the BOLD approach: Applications. In D. LeBihan (Ed.), *Diffusion and Perfusion: Magnetic Resonance Imaging*, pp. 351-62. New York: Raven.
- [221] Schneider, W., Casey, B. J., & Noll, D. (1994). Functional MRI mapping of stimulus rate effects across visual processing stages. *Human Brain Mapping*, 1, 117-33.